© 2002 American Chemical Society, J. Phys. Chem. A, Shkrob jp021494K, Supporting Info Page 1

SUPPLEMENTARY MATERIAL **JP021494K**

Journal of Physical Chemistry, Received June 25, 2002

Supporting Information.

1S. Experimental setup and procedures.

1S.1. The design of radiolytic cells.

Cell-1. The flow cell used in this study was similar to the dc conductivity cell used in ref. 4 (see the Supporting Information of ref. 4). The sketch of this 26.4 mm optical path, 5 cm^3 inner volume cell is given in Figs. 1S and 2S. If not stated otherwise, the material is 316 stainless steel. A ceramic cell is embedded inside a 2" x 2.3" x 2.5" pressure vessel operable at pressure below 240 bar and temperature below 80°C. The temperature is controlled using four 10 W cartridge heaters inserted into the wells at the perimeter of the vessel (Fig. 1S). A flexible T-type thermocouple probe is inserted in the well at the center of the vessel reaching within 0.1" of the inner wall (Fig. 1S). The vessel temperature was regulated using a proportional CN4401TR-D autotune process controller (Omega). An air-blowing fan provided a heat sink. Analyzing light from a Xe arc lamp enters the vessel through two 3/8"-thick, diameter 1" Suprasil windows (Fig. 2S). Two 3/8"-thick 2 mm x 5.1 mm stainless steel apertures are used to mask the analyzing light and to collimate the electron beam, as shown in Fig. 2S.

The sc CO_2 solution flows via two 1/16" NPT ports (Fig. 1S). The cylindrical cell (OD 0.695", ID 0.6", 1.06" long) is machined from glass-mica ceramics; this cell lines the round cutout at the center of the pressure vessel (Figs. 1S and 2S). The electric field is contained between two 8 mm x 26.4 mm x 2.5 mm steel electrode plates. Each electrode plate is fastened to a high-voltage (HV) lead cemented to a ceramic feed-through using TorrSeal epoxy glue (Varian). The feed-through is sealed using a teflon O-ring; the pressure is applied using a threaded steel pusher whose upper part adapts to the standard SHV plug. A teflon bushing is used to electrically insulate the HV lead from the pusher. The bottom electrode is pressed against the bushing made of aluminum; this electrode is at the same potential as the (grounded) vessel.

Cell-2. In other experiments (in particular, with static samples), a 50 mm optical path cell was used. [1,2,3] This three-port cell is sketched in Fig. 3S. The inner diameter of the cell is 12.5 mm, and the inner volume is 13.4 cm^3. This cell can be operated to 300 bar. Three diameter 30 mm, 10 mm - thick Suprasil windows are pressed against No. 114 teflon O-ring seals using steel pushers fastened to the vessel using eight M4 x 20 mm screws. Hard fiber washers were inserted between the window and the pusher to protect the windows from cracking (these washers are not shown in Fig. 3S). Typically, the analyzing light and the electron beam were collinear. In some experiments, these beams were perpendicular (the electrons entered through the side port). For dosimetry measurements (see below), a 8 mm thick steel aperture with a 2 mm x 5 mm cutout was inserted in the front window pusher to collimate the electron beam.

The temperature was monitored using a diameter 1/8" T-type jacket-grounded thermocouple immersed into the solution using an NPT 1/4" port at the top of the cell. The tip of the thermocouple was 1 mm above the optical tunnel. The temperature was controlled

© 2002 American Chemical Society, J. Phys. Chem. A, Shkrob jp021494K, Supporting Info Page 2

using a Thermolyne BIH051020 heating tape wrapped around the vessel; air was blown on the vessel to provide a heat sink. The solution flowed through two NPT 1/16" ports at the rear of the cell, as shown in Fig. 3S.

1S.2. Electron beam profiles and dosimetry.

Radiation dosimetry of supercritical fluids has not been done before, and our study was marred by difficulties encountered when common approaches were implemented. As similar problems are likely to be encountered by other researchers, we give an overview of these problems and the solutions found.

Beam mapping. One of the problems in using the high-pressure cells is that the dose deposition in these cells is very inhomogeneous. This inhomogeneity is caused by (i) electron stopping by the sample and (ii) scattering of the electron beam by the cell windows (that need to be thick to withstand the high pressure). Due to the nonuniformity of the dose deposition, the loss of cations caused by electron-hole recombination in sc CO_2 varied strongly across the cell. Consequently, mapping of the radiation field is required for accurate measurements of the radiolytic yields.

At first glance, this problem can be circumvented by shortening the optical path of the cell: the shorter the cell, the more uniform the radiation field. Unfortunately, there are two formidable obstacles. First, in order to obtain acceptably large transient absorbances at reasonably low radiation doses, *the optical path should be long.* In sc CO_2, typical ΔOD_λ for a 20-60 Gy pulse in a 50 mm cell is $(1\text{-}15)\times10^{-3}$, and shortening the optical path to several millimeters reduces the optical signal to the shot noise level. Second, the thick Suprasil windows used in our cell design yield large absorbance signals $\rightarrow\sim (5\text{-}50)\times10^{-3}$ that must be subtracted. To this end, for every observation wavelength and radiolytic dose, the kinetic traces obtained with 1 bar of CO_2 in the cell were subtracted from the traces obtained for the cell filled with the sample. If the cell is short, the doses absorbed by the rear window with the liquid sample and without this sample are different, which results in a large subtraction error. Therefore, when the 0° detection scheme is used, the cell must be sufficiently long so that no beam reaches the rear window. In the 90° detection scheme (where the analyzing light is crossed with the electron beam) the windows can be placed outside the radiation zone, and the radiation-induced transient absorbance in the windows is negligible. However, due to short effective optical path of the analyzing light in this arrangement, the 90° scheme is unsuitable for accurate kinetic measurements of weak absorbance signals. The only practical solution was to use the 0° detection scheme and to map the dose distribution. [We forewarn the reader against using sapphire windows for the 0° detection in pulse radiolysis experiments. Though thin sapphire windows (1-3 mm) can be used instead of the 10 mm thick suprasil windows, these windows yield 3-5 times stronger absorbance signals than the suprasil windows, and some of this absorbance persists. Furthermore, impurity centers in commercial sapphire strongly luminesce when the window is irradiated.]

The following mapping procedure was used: 1.2 mm thick, flat borosilicate glass plates were cut into 8 mm wide, 20 to 50 mm long slabs. These glass slabs were inserted between the electrodes (in cell-1) or mounted horizontally or vertically inside cell-2. Three sets of measurements were carried out: in air, in the cell filled with liquid *n*-hexane, and (for cell-2 only) for the glass slab squeezed between two nylon half-cylinders that snugly slide into the cell. In some experiments, a 8 mm thick 2 mm x 5 mm steel aperture was placed next to the front window to collimate the electron beam. These glass slabs were exposed to 10-300 electron pulses (120 nC) from 20 MeV Argonne linac; the repetition rate

© 2002 American Chemical Society, J. Phys. Chem. A, Shkrob jp021494K, Supporting Info Page 3

of the pulses was 0.3 Hz. Irradiation of the borosilicate glass results in coloration due to the formation of alkali electron centers. The irradiated slabs were mounted on a vertical Parker model 1740M3 manual stage that was in turn mounted on a Unislide-Velmex ZB4039P6J translation stage equipped with a Velmex 86 mm controller-driver; this horizontal translation stage was controlled by a Macintosh IIc computer. The slabs were then scanned, with 0.1 mm resolution, using an Edmund Industrial Optics Model L53-227 633 nm, 1 mW laser diode module. The 5 mm x 2 mm beam of this diode laser was focused to a 5 mm x 50 μm line using a 15 cm focal length cylindrical lens. The light passing through the glass slab was imaged on an Electro-Optics Technology model ET2000 photodiode using a 10 cm focal length lens. The diode signal was filtered and amplified using a Stanford Research Instruments model 235 analog processor and digitized using a National Instruments NB-MIO-16H board on the same computer. Each glass slab was scanned horizontally along the path of the electron beam (at the midsection) and then placed vertically and scanned across as the slab was translated vertically in steps of 5 mm. Every scan was done twice: first, with the laser beam perpendicular to the glass plate and then at an acute angle, to suppress interference fringes. The first scan was used to obtain the horizontal scale for the second scan. The transmission of the sample at 633 nm was calculated and the absorbance plotted as a function of the horizontal displacement. The main complication is that the optical absorbance does not scale linearly with the radiation dose for long exposures. Thus, the glass plates were irradiated at several doses and the absorbances normalized by the dose. We used only those profiles that scaled with the dose (at high radiation doses, only "tails" of these profiles linearly scale with the dose). Typical profiles are given in Fig. 7S(a).

Using this mapping procedure, we found that with our standard beam-focusing settings the lateral dose distribution in the cell can be approximated by the product of two Gaussian functions (Figs. 8S(a) and 8S(b)),

$$D(x,y) = \exp(-[x/\sigma_x]^2) \exp(-[y/\sigma_y]^2), \qquad (1S)$$

where x is the vertical and y is the horizontal axis (the long side of the 2 x 5 mm steel collimator is horizontal, see Fig. 1S and Fig. 8S). For cell-2, σ_y is 4.08 mm with and 6.36 mm without the beam collimator, respectively; this σ_y does not depend on the beam depth z. In the vertical plane, the beam diverges by 14.4°, and σ_x increases by 0.25 mm per mm of the depth (Fig. 8S(c)). At the front window, σ_x is 3.48 mm with and 7.0 mm without the beam collimator, respectively. For cell-1, the y-distribution is the same as for cell-2 with the beam collimator inserted. The z-distributions for cell-2 are shown in Fig. 7S. The profiles in air and *n*-hexane (ρ=0.66 g/cm^3) are the same; for nylon (ρ=1.1 g/cm^3) the z-distribution is narrower. Even in air, only 5% of the electrons make it to the rear window (Fig. 7S(a)); in nylon, all electrons are stopped 10 mm before the rear window. Insertion of the beam collimator narrows the z-distribution ca. 2 times. Using these z-distributions and the D(x,y) distribution given by eq. (1S), we obtained laterally averaged z-distributions (thin solid lines in Fig. 7S(b)) and the volume-average dose. Taking the dose at x=y=z=0 as unity, the average dose for cell-2 is 0.142 with and 0.268 without the beam collimator (in nylon). In air, the average dose is 0.352 for cell-1 (with the collimator) and 0.28 for cell-2 (no collimator). As shown in Fig. 9S(a), when z is scaled by the cell length L (26.4 mm for cell-1 and 50 mm for cell-2), the z-distribution in cell-1 is actually wider than in cell-2.

Absolute dose. To obtain absolute *average* dose, we used aqueous thiocyanate dosimeter. [15] The cells were filled with an O_2-saturated 10 mM solution of KSCN in nanopure water. This sample was irradiated with 1-5 electron beam pulses. Transient absorbance kinetics for $SCN^{\bullet -}$ at 500 nm in the first 160 μs following the 4-20 ns pulse

© 2002 American Chemical Society, J. Phys. Chem. A, Shkrob jp021494K, Supporting Info Page 4

were observed (Fig. 10S(a)). For t<0.2 ns there is a short-lived "spike" from the hydrated electron; for t>0.5 μs, the kinetics can be approximated by a sum of two exponentials (Fig. 10S(a)). The biexponential section of the kinetics was back extrapolated to t=0, and the extrapolated absorbance at t=0 was used to calculate the average dose. In this calculation, the $G\varepsilon_{500}$ of 21,516 M^{-1} cm^{-1} $(100\ eV)^{-1}$ given by Buxton and Stuart [15] was used, and the optical path was taken as the cell length (see below). For cell-1, extrapolated ΔOD_{500} was linear with the beam charge to 130 nC, yielding slope of 0.88 Gy/nC. For cell-2, extrapolated ΔOD_{500} was linear with the pulse charge to 75 nC (Fig. 10S(b)), and the initial slope was 0.81 Gy/nC without and 0.33 Gy/nC with the beam collimator. Thus, placement of the collimator reduces the average dose by 60%.

These, of course, are *time-integrated* average doses. To obtain the time profile of the dose deposition we assumed that this profile is the same as the Cerenkov emission from the sample. This emission was sampled with 0.2 ns resolution using a fast FND-100Q photodiode and the kinetics were integrated numerically (Fig. 11S(a)). The flat part of the integrated kinetics was taken as the total dose. This "Cerenkov dosimeter" is very linear with the pulse charge. Using the total dose obtained from the thiocyanate dosimetry, it is possible to obtain the absolute time-dependent *average* dose. To compare theory with experiment, a guess for the accumulated electron-hole pair yield $g(t)$ in sc CO_2 should be made (this quantity is proportional to the accumulated dose). We assumed, following Dimitrijevic et al., [1,2] that the dose (J/kg) deposited in the sc CO_2 sample is the same as that deposited in the thiocyanate dosimeter. We further assumed that the yield of the primary electron-hole pairs is 5 pairs per 100 eV of absorbed energy; this estimate is consistent with the Monte-Carlo simulations discussed in section 2S.2.

Figs. 11S(b) and Fig. 12S show the *average* yield $\langle C\rangle$ of the solvent radical cation as a function of *average* yield $\langle g\rangle$. The cation yield was obtained by dividing the experimental ΔOD_{900} by the cell length and the extinction coefficient ε^{+}_{900} of the solvent radical cation (obtained in section 3.1). All of these plots can be fit with the same power dependence, $\langle C(t)\rangle = \alpha' \langle g(t)\rangle^{\sigma}$, where α' is a coefficient that varies with the experimental conditions (Fig. 12S), while σ=0.607±0.006 remains constant (Fig. 11S(b)). As shown in section 2S.2, this power dependence is due to cross recombination of e_{qf}^- with the cations generated by the pulse; in the simplest case of instant geminate recombination, the theory gives $\sigma \approx 0.5$ (section 3.3). It is easy to see that if $C \propto g^{\sigma}$, then $\langle C\rangle \propto \langle g\rangle^{\sigma}$. Assume that $C = \alpha g^{\sigma}$ and the beam profile is given by D(z), so that $g(z) = g(0)\ D(z)$ and $C(z) = \alpha\ [g(z)]^{\sigma}$. Then, $\langle C\rangle = \alpha' \langle g\rangle^{\sigma}$, where

$$\alpha'/\alpha = \int_0^L dz\ [D(z)]^{\sigma} / \int_0^L dz\ D(z) \qquad (2S)$$

and L is the cell length. This formula can be generalized for all three dimensions. Since D(z) is different for different cells and the focusing and collimating conditions, the coefficient α' changes from one measurement to another. The magnitude of these variations can be estimated assuming an exponential dependence for the beam profile, $D(z) = \exp(-\gamma_z z)$. The integration of eq. (2S) gives

$$\alpha'/\alpha = \{[1- \exp(-\sigma\gamma)]/(\sigma\gamma)]\}/\{[1-\exp(-\gamma)]/\gamma]^{\sigma} \qquad (3S)$$

where we introduced a dimensionless parameter $\gamma = \gamma_z L$. For $\gamma \to 0$, $\alpha'/\alpha = 1$. For $\sigma < 1$, $\alpha'/\alpha < 1$ *decreases* with γ. For $\gamma < 10$, the correction is small: For σ=0.5, α'/α=0.9 for γ=3.6 and 0.78 for γ=6.2, (these estimates for γ were obtained by exponential fitting of the

© 2002 American Chemical Society, J. Phys. Chem. A, Shkrob jp021494K, Supporting Info Page 5

beam profiles shown in Figs. 7S and 9S(a)). Using the experimental distribution D(x,y,z), it is possible to calculate ⟨C⟩ vs. ⟨*g*⟩ for different cells and irradiation conditions. In these calculations, we used the theoretical C(*g*) dependence given in Fig. 9S, trace (i) (see section 2S.2 and Fig. 19S for more detail). Fig. 9S(b) shows the calculation for cell-1 (with the beam collimator), trace (ii), and cell-2 (without the beam collimator), trace (iii), in which the dose distribution in air (same as in *n*-hexane) was used. It is seen that the spatial averaging underestimates the solvent radical cation yield by 15% for cell-1 and 10% for cell-2. For the nylon-filled cell-2, the correction is greater: 20% without the beam collimator and 27% with the beam collimator. Perhaps, measurements for *n*-hexane ($\rho \approx 0.66$ g/cm^3) are more representative of the dose deposition in sc-CO_2 ($\rho \sim 0.7$-0.83 g/cm^3) than such measurements in nylon ($\rho = 1.1$-1.2 g/cm^3). The conclusion is that due to inhomogeneous deposition of beam energy, the *average* cation concentration for a given *average* dose is 10-15% smaller than the cation concentration for the same dose in an infinitely thin sample.

As seen from Figs. 11S(b) and 12S, the theoretical curve is close to the experimental ⟨C⟩ vs. ⟨*g*⟩ dependence obtained for cell-1 and cell-2 with the beam collimator present. On the other hand, the curve obtained for cell-2 without the beam collimator (Fig. 12S), exhibits cation concentrations that are 40% *greater* than the theoretical ones. As shown above, spatial averaging results in *lower* rather than *higher* cation concentrations as a function of average dose, and this discrepancy cannot be due to different dose distributions (though there is such a difference, see Figs. 7S and 9S(a)). We traced the problem to the propagation of the analyzing light from a Xe arc lamp through cell-2. [Again, this must be a common problem, as we used the standard lamp and usual design for the high-pressure optical cell].

To obtain maximum throughput through this 50 mm - long cell, the light of the Xe arc lamp (equipped with an elliptical reflector) has to be focused at the rear end of the cell. At the focal point, the beam is 17 mm in diameter, and the divergence of the beam past this point is 12-13°. For cell-2, the light passing through a 50 μm pinhole placed at the center of the rear window makes a 13 mm image at the cell front, whereas the inner diameter of the cell is 12.5 mm. As a result, light bounces off the cell walls, and masking the light at the rear end does not fully prevent the unwanted reflections from pasing through the optical 50 mm cell. Photometry showed that ca 20% of the 600 nm light is reflected by the cell walls. The long-path, narrow-slit steel beam collimator serves as a light mask that removes this reflected light out. Without the collimator, the optical path of the analyzing light is considerably longer than the cell length, and both the average cation concentration ⟨C⟩ and the average dose ⟨*g*⟩ are overestimated. This would not be a problem, as far as the G-value measurements are concerned, if these two quantities were linearly related. However, since ⟨C⟩ is a non-linear function of ⟨*g*⟩, this overestimation results in increased slope of ⟨C⟩ vs. ⟨*g*⟩. We found that any improvement in the analyzing light collimation brings the concentration plot towards the theoretical line.

Absorption in the cell windows. Typical transient absorption kinetics from the irradiated cell windows at 550, 750, and 900 nm are shown in Fig. 13S(a), and the VIS spectrum of this absorption is shown in Fig. 13S(b). These kinetics were subtracted from the absorbance kinetics obtained for the sample-filled cell, as discussed above. Note that these kinetics change with the wavelength, becoming longer at shorter wavelengths. After the first 1 μs, the kinetics are flat, slowly decaying with $t_{1/2}$ of 200 ms. When a 30 Hz burst of 7.6 ns fwhm, 75 nC pulses is used, the window absorbance reaches a steady-state

© 2002 American Chemical Society, J. Phys. Chem. A, Shkrob jp021494K, Supporting Info Page 6

level, persists for 300 ms, and then decays in 500 ms. The typical steady-state window absorbance at 550 nm is $2x10^{-3}$.

For cell-2 filled with 1 bar of CO_2, the absorption from the rear window comprises ca. 9.5% of the total absorbance (Fig. 13S(a); Fig. 7S(a) suggests that ca. 5 % of the electrons hit the rear window in the air-filled cell). For cell-1, ca. 9.1% of the window absorption is from the rear window. No correction for this rear window absorbance has been made. Judging from nearly zero absorbances in the red obtained for sc CO_2 solutions containing hole scavengers, the subtraction of the window absorbances at 700-1500 nm is accurate to 2%.

Since the "permanent" absorbance of the neutral product is small ($\Delta OD < 5x10^{-3}$), and the spectrum observed in the 450-800 nm region is similar to that of the suprasil cell window we took pains to prove that this "permanent" absorbance is not an artifact of the subtraction routine. Several lines of evidence suggest that this absorption signal is genuine: (i) in the 330-450 nm region, the spectrum of the product strongly differs from that of the cell window (Fig. 13S(b)), (ii) the same 550 nm band was observed using the 90° detection scheme (Fig. 14S), (iii) the long-term kinetics of the window absorbance and the product absorbance are different, (iv) these kinetics change upon the addition of solutes (section 3S and Fig. 35S(b) therein), and (v) the window absorbance and the product absorbance have different accumulation dynamics when the sample is irradiated with a 30 Hz burst of electron pulses (while the window signal reaches a steady-state level and then decays, the product absorbance steadily increases with the number of pulses; see Fig. 38S(a), traces (iv) and (v), in section 3S).

1S.3. Experimental procedures.

The electric setup. The typical experimental setup for electric field experiments is given in Fig. 4S. In most experiments, the electric field was 25 kV/cm. Constant high voltage (< 5 kV, < 3 mA) was provided by a home-built low-ripple HV power supply; the field was remotely turned on and off using a solid-state relay controlling the step-up transformer. The HV was passed through a 1 kΩ, 0.1 μF RC-filter. This filter protects the power supply and stabilizes the electric field during the linac pulse. At 5 kV, the 0.5 mC charge stored in the 0.1 μF capacitor is much greater than the charge in the electron beam pulse (< 120 nC), so the maximum drop in the voltage caused by 20 MeV electrons stopped in the electrode plates is negligible. Even if the electric resistance of the sc CO_2 solution were zero during the pulse, the drop of the voltage within the first 1 μs after this pulse would be less than 1 %. Still, there is a possibility that the voltage is divided between the shunt resistor in the RC filter and the transient resistance in the cell. In our pulse radiolysis experiments, the ion yield per pulse is ~ 1 μM and the mobility of the ions is less than 0.02 cm^2/Vs; therefore, the dc conductivity of the radiolysate is less than 2 μSiemens/cm. Given the electrode area of 2.1 cm^2 and the electrode gap of 2 mm, the transient resistance of the solution is greater than 50 kΩ. Thus, the 1 kΩ resistor in the filter cannot account for more than 2 % drop in the voltage after the electron beam pulse. To ascertain that, we introduced inductive and resistive probes in the circuit before the cell. No transient signal was observed during the pulse. Apparently, the voltage drop is negligible, and the reduced electric field effect observed in our experiment is due to the peculiarities of recombination dynamics (section 2S).

When the high voltage is turned on, the solution is perturbed due to electric forces acting on the electrode plates. We found it necessary to wait for 20-30 s to stabilize the solution; the same period of time elapsed before making kinetic measurements, after turning the electric field off. During the measurement, eight series of the transient absorbance

© 2002 American Chemical Society, J. Phys. Chem. A, Shkrob jp021494K, Supporting Info Page 7

kinetics were obtained. Using "1" for the electric field ON and "0" for the electric field OFF, the acquisition sequence was (1,0,0,1,1,0,0,1). Such a sequence minimizes the adverse effects of the sample decay and the radiolytic product generation. Typically, the average of 5-10 kinetics obtained with the field OFF was subtracted from the average of the kinetics with the field ON, as specified by the acquisition sequence. The electric field effect scaled linearly with the field (Fig. 15S(b)).

Radiolysis and Optical setups. The pulse radiolysis - transient absorption setup used in this work was similar to that used in refs. 1, 2, and 3. 20 MeV electron pulses with *nominal* pulse widths of 4 to 50 ns were used to irradiate the sample. Typically, 5 ns fwhm ("4 ns" pulse) and 7.6 ns fwhm ("10 ns" pulse) electron pulses of 30 and 75 nC, respectively, were used (the doses per charge are given in the previous section). These short pulses (4 and 10 ns) are nearly Gaussian, longer pulses (20 to 50 ns) have extended "tails" (e.g., trace (iii) in Fig. 11S(a)). The analyzing light source was a 75 W Xe arc lamp powered using a PTI LPS-220B power supply that was pulsed for 300 μs to increase the light output 100-fold. Wavelength selection between 390 and 1000 nm was done using a set of 40 nm fwhm band pass interference filters. InGaAs (Germanium Power Devices Corporation model GAP520, biased at -5 V) and silicon (EG&G model FND 100Q, biased at -50 V) photodiodes were used for light detection in the 900-1600 nm and 400-1000 nm ranges, respectively. For 900 nm, the kinetics obtained using these two photodiodes were identical. The photodiode signal was passed through a 250 MHz filter, terminated into a 50Ω load and acquired using a Tektronix TVS-645A transient digitizer. For λ >1 μM, the diode signal was amplified by 20 dB using a Comlinear CLC 100 video amplifier before the acquisition. For long-term (> 100 μs) kinetic measurements, the diode output was terminated into a 1-10 kΩ variable resistance load, passed trough a 20 MHz filter, and acquired using the same digitizer. In some experiments (> 10 ms), a 30 Hz burst of 5 to 50 "10 ns" pulses was used to build up the concentration of long-lived products.

High-pressure setup and sample preparation (Figs. 5S and 6S). Standard low-volume HPLC equipment was used where possible. The high-pressure transfer lines were made of 1/16" OD x 0.03" ID stainless steel tubing (Alltech); the connectors, reducers, and unions were low- or zero-volume 1/16" Swagelock; low-volume shut-off and switching valves (Supelco) were used for flow regulation. SFC-grade carbon dioxide from Scott Speciality Gases was passed through 1.5 m of 1/16" tubing rolled inside a heat exchanger cooled to -15°C by chilled ethylene glycol circulated from a Forma Scientific Masterline model 2095 cryogenic bath. This exchanger was mounted on the pump head of a JASCO model PU-980 HPLC pump (0.1-10 cm^3/min). Cooling the CO_2 improves the compression efficiency. The pressure in the vessel was measured with a model K1, 3000 psi pressure transmitter (Cole-Parmer) and digitized using a model DP25-E-A digital pressure meter (Omega). An SSI LO-Pulse damper was used to reduce the pump pulsations. Before the solutions entered the pressure vessel, the liquid was passed through a pre-heater: 2 m of 1/16" tubing placed inside a diameter 1/4" flexible pipe through which hot water was circulated from a Neslab RTE-100LP bath. The temperatures of the bath and the pressure vessel were matched within ±0.1°C. In static experiments (for cell-2 only), the outlet shut-off valve (V1 in Fig. 5S) was closed during the compression; it was used only for expansion of the solution. Typically, the solute was injected in flow when the pressure inside the vessel was 70-80 bar. For experiments in flow (needed to remove radiolytic products, such as CO and O_2), valve V1 was open and a proportional relief valve (NUPRO Model R3A) set for the desired pressure used for purging CO_2. We found it important to control the temperature of this relief valve as it cools down as the sc CO_2 expands, introducing instability of the flow. To this end, the valve was heated using a Thermolyne BIH051020 tape energized by a Minitrol PL-312 heat controller (Glas-Col). We found that for pressures below 120 bar, the turbulence and schlieren caused by the temperature and

© 2002 American Chemical Society, J. Phys. Chem. A, Shkrob jp021494K, Supporting Info Page 8

pressure gradients in the flowing sample was unacceptably strong. At higher pressure, the solvent density and the refraction index depend weakly on the temperature and the pressure. For pressures between 160 and 200 bar, the schlieren was negligible. Typically, the sc CO_2 solution was flowed at 180-220 bar at a flow rate of 2-3 cm^2/min; the internal volume of the pressure vessel was 5 cm^3 (cell-1).

In most scavenging experiments, the solutes were added to a static sample in cell-2. Liquid solutes were purged with CO_2 and injected in a 5-20 μL loop of a Rheodyne 7725 HPLC injector. Gas solutes were injected using a Rheodyne 7010 injector placed downstream of the first HPLC injector. 20 μL or 200 μL sample loops were used in the injector. The gases were obtained from AGA (the highest grade available), other chemicals were obtained from Aldrich. With gaseous solutes, it was important to minimize dead volume between the cell and the outlet shut-off valve V1 (Fig. 5S): the low-pressure gas is flushed into this dead volume by incoming compressed CO_2. Injecting gas in-flow, using an HPLC injector (INJ2 in Fig. 5S) solves this problem; however, only low concentrations of the solute (< 10 mM) could be obtained this way. To obtain higher concentrations, the solute gas was let into the cell and mixed with 10-20 bar of CO_2; this solution was then compressed by letting sc CO_2 in. In scavenging experiments with H_2, very large concentrations of this gas were added (to 3.7 M). These solutions were prepared by first letting 1-100 bar H_2 in the cell and then pumping sc CO_2 in the cell. The final pressure was chosen so that the partial pressure of CO_2 was 200 bar. For higher H_2 concentrations, it takes 10-20 min for the solution to become homogeneous; for $[H_2] > 4$ M, the solution remains phase separated. In experiments where O_2 was added to the H_2/CO_2 mixture, special care was taken to avoid pressure regimes that are near the explosive threshold for the H_2/O_2 mixture. No electric field experiments on the $O_2/H_2/CO_2$ ternary mixtures were carried out, due to safety concerns.

For the electric field experiments with gas mixtures, the flow setup was modified as shown in Fig. 6S. The following procedure was used: First, the 500 cm^3 steel bottle (that was temperature-controlled at 41°C) was purged with the solute gas (valve SV1 in position 2 and valve V2 open) and the gas was equilibrated at the desired pressure, with valve V2 closed. Then the bottle was connected to the HPLC pump (valve SV1 in position 5) and valve SV2 was configured to connect ports 1 and 6. CO_2 was pumped into the bottle until a pressure of 170 bar was reached, and then the solution was equilibrated for 1 h. After this equilibration, valve SV1 was put in position 1, valve SV2 configured to connect ports 1 and 2, and the mixture from the bottle was flowed through cell-1 at the rate of 2 cm^3/min using the HPLC pump (so that the pressure inside the cell was 200-215 bar). The 500 mL sample lasted for ~ 1.5 h. When the pressure decreased to 130-140 bar, the solution was discarded and the whole procedure repeated. In the electic field experiment with the H_2 solution (46 bar H_2 compressed by addition of sc CO_2 to the total of 220 bar), one filling of the bottle was sufficient for 30-40 min of work; as the pressure decreased below 180 bar, the mixture inside the bottle phase-separated.

Radiolytic degradation of the solution. Even with flow, continuous irradiation of the flowing sample during the kinetic averaging causes some accumulation of radiolytic products in the cell. Our experiments show that the life time of the solvent radical cation strongly depends on the rate of the product removal. After a while, the concentration of the products reaches a steady-state level, and the kinetic profiles do not change. All of the kinetics reported herein were obtained under these steady-state conditions. Complete elimination of the radiolytic products, by increasing the flow rate and/or reducing the repetition rate of the pulses, is impractical. Increasing the flow rate above 6-8 cm^3/min causes turbulence and light scattering. Decreasing the repetition rate below 0.1 Hz slows

© 2002 American Chemical Society, J. Phys. Chem. A, Shkrob jp021494K, Supporting Info Page 9

down the signal averaging. As a compromise, we flowed the solution at 2-3 cm^3/min for cell-1 (5 cm^3 total volume, 0.42 cm^3 irradiated volume) and at 4-6 cm^3/min for cell-2 (13.5 cm^3 total volume), and pulsed the linac at repetition rate of 0.3 Hz. Under these conditions, the typical "natural" life time of the solvent cation (see below) is 100 ns.

In static experiments, we averaged 3-5 shots and then replaced the sample. Under these static conditions (cell-2), the rate constant k_1 of pseudo first order decay of the solvent radical cation (eq. 2 in section 3.1) linearly increases with the number of electron pulses, by $2.8x10^5$ s^{-1} per a "10 ns" (84 nC, 67 Gy) electron pulse (Fig. 16S). It is reasonable to assume that the solvent cation is scavenged by the products of CO_2 decomposition, such as CO and O_2. Using the scavenging constants for CO and O_2 given in Table 1, one obtains that 1 μM of decomposed CO_2 accounts for the increase in k_1 by $3.2x10^4$ s^{-1}. To explain the observed shortening of the solvent cation lifetime, 8.75 μM of CO_2 should be decomposed per pulse, which is equivalent to 1.5 $(100\ eV)^{-1}$. Under atmospheric pressure, the G-value for CO formation in neat CO_2 is ≈4.5 $(100\ eV)^{-1}$ (a higher estimate of 7.4±0.4 $(100\ eV)^{-1}$ was obtained in the high-dose regime). [12a] At 50°C and 111 bar, this G-value is 2.7 $(100\ eV)^{-1}$. [12b] At this temperature, the yield of CO rapidly increased with the solvent density, from 0.5 $(100\ eV)^{-1}$ for ρ=0.2 g/cm^3 to 3 $(100\ eV)^{-1}$ for ρ=0.65 g/cm^3. [12b] Perhaps, under our experimental conditions the yield of CO is 3-4 $(100\ eV)^{-1}$. If the decay of the solvent cation were mainly due to reaction with CO, the observed increase in the decay rate would correspond to the radiolytic yield of CO of 3.8 $(100\ eV)^{-1}$, which is close to this estimate. A possible rationale for the supposed inefficiency of the radiolytically generated O_2 is that the $O(^3P)$ atoms released in the decomposition of CO_2 [1,12] mainly react with impurity (at low accumulated dose) and/or secondary radiolytic products (at high accumulated dose) yielding, instead of O_2, a stable product that scavenges the solvent cation inefficiently. Ozone could be such a product. The latter is known to form in radiolysis of sc CO_2, and rate constant of $3.6x10^9$ M^{-1} s^{-1} was obtained for the $O(^3P) + O_2$ reaction at 40°C and ρ=0.66 g/cm^3. [1] The concentration of the O_2 impurity in pre-irradiated CO_2 was 20 μM (0.5 ppm); [4] this is sufficient to scavenge oxygen atoms in 150 μs. Whether this explanation is correct, it is clear that the yield of radiolytic products projected from the previous analyses is more than sufficient to account for the observed shortening of the solvent cation lifetime with the accumulated dose.

Impurity and the solvent cation lifetime. Our data suggest that the lifetime of the (isolated) solvent cation is mainly controlled by impurity. Although reactions with radiolytic products are important, these reactions cannot account for the short lifetime of the solvent cation observed under high-flow, low repetition rate conditions and in single-shot experiments:

The maximum flow rate we were able to obtain for cell-1 without introducing schlieren was 6 cm^3/min. For this 5 cm^3 cell, 1.2 cell volume per minute is replaced at this flow rate. Even when the kinetics were obtained at this high flow rate and slow repetition rate of 50 mHz, the kinetic traces for the solvent cation showed the same mixed second (with rate constant k_2) and first (with rate constant k_1) order decay kinetics (Fig. 8(a)) as were observed for slower flow rates and faster pulse repetition rates. The only difference was that the "natural" lifetime of the solvent cation (defined as k_1^{-1}) increased from 80-100 ns to 130-160 ns. We have never succeeded in observing the "natural" lifetime longer than 150-160 ns. Actually, this lifetime varies from one batch of sc CO_2 to another and, for "bad" batches, can be as short as 30-50 ns. These batch-to-batch variations suggest that the pseudo first order decay of the solvent cation is due to a reaction with impurity in sc CO_2.

© 2002 American Chemical Society, J. Phys. Chem. A, Shkrob jp021494K, Supporting Info Page 10

Judging from the several batches obtained from Scott Specialty Gases, there is no correlation between the purity levels given by this manufacturer and the solvent cation lifetimes observed in our experiments. It would require > 6.3 ppm of O_2 to observe the lifetime < 160 ns. The company certifies that CO_2 contains < 2 ppm of H_2, CO, and O_2, < 20 ppm of N_2, and < 0.5 ppm of water. From our photoconductivity experiments, typical concentrations of O_2 in these batches is 0.5 ppm. [4] N_2 is unreactive towards the solvent radical cation, and H_2 and CO_2 react too slowly. Water, on the other hand, should be quite reactive. We observed that for "bad" sc CO_2 batches, passing the solvent through a cryotrap increased the cation lifetime 2- or 3-fold, although never over 160 ns. It is our conclusion that the concentration of water certified by the manufacturer is grossly underestimated. We suppose that this concentration is at least 10-15 ppm.

© 2002 American Chemical Society, J. Phys. Chem. A, Shkrob jp021494K, Supporting Info Page 11

2S. Appendix: Electric field effect on the solvent cation yield.

2S.1. Analytical treatment of the "instantaneous" field effect.

We first examine a situation when the geminate kinetics of the electron-hole recombination is very fast and the electric field effect develops "instantaneously" on the time scale of the experimental observation. Let E be the concentration of the free electrons, G(t) be the generation rate for these electrons, I be the concentration of the solvent anions (i.e., trapped electrons), and k_2 be the rate of bimolecular electron-hole recombination. Neglecting the recombination of the solvent anions on the short time scale, we obtain

$$dE/dt = G(t) - E/\tau_e - k_2 E (E+I) \quad (A1)$$

$$dI/dt = E/\tau_e \quad (A2)$$

Consider first the "instantaneous" formation of electrons, $G(t)=E_0 \delta(t)$, where E_0 is the initial concentration of the free electrons by the time when the geminate recombination is over, and $\delta(t)$ is the Dirac function. Let us introduce dimensionless parameters $e=E/E_0$, $i=I/E_0$, $q=k_2\tau_e E_0$, and $\tau=t/\tau_e$. Eqs. (A1) and (A2) may be then rewritten as

$$de/d\tau = -e - q\, e\, (e+i) \quad (A3)$$

$$di/d\tau = e \quad (A4)$$

Introducing the reduced concentration c of the cations, $c = e + i$, we obtain, by summing up eqs. (A3) and (A4)

$$dc/d\tau = - q\, e\, c \quad (A5)$$

or

$$d\,[\ln c]\,/d\tau = - q\, e \quad (A6)$$

Integrating both parts of eqs. (A4) and (A6) from zero to infinity yields

$$c_\infty = \exp(-q\, c_\infty) \quad (A7)$$

where c_∞ is the final concentration of the solvent ions for $t\to\infty$. Therefore, $c_\infty=F(q)$, where the function F(q) is the solution of equation (A7) for a given q. The molar concentration C_∞ of the cations at $t\to\infty$ is given by $C_\infty \propto q\, F(q)$. Suppose that the electric field increases the free electron yield E_0 by a factor of $(1+\beta)$ and $\Delta E_0/E_0 = \Delta q/q \approx \beta \ll 1$. The observed change in the yield of cations C_∞ will be

$$[\Delta C_\infty/C_\infty]/\beta \approx \partial[\ln\{qF(q)\}]/\partial \ln q \quad (A8)$$

Since $\partial F/\partial q=-F^2/(1+qF)$,

$$[\Delta C_\infty/C_\infty]/\beta \approx [1 + qF(q)]^{-1} = [1 + k_2\, \tau_e\, C_\infty]^{-1} \quad (A9)$$

The rate constant k_2 of the cross-recombination is given by the Debye formula, $k_2=F\mu_e/\varepsilon\varepsilon_0$, where $F=eN_{av}$ is the Faraday constant, e is the elementary charge, N_{av} is the

© 2002 American Chemical Society, J. Phys. Chem. A, Shkrob jp021494K, Supporting Info Page 12

Avogadro number, ε is the static dielectric constant of the solution, ε_0 is the permittivity of vacuum, and μ_e is the electron mobility. Thus, we obtain

$$[\Delta C_\infty/C_\infty]/\beta \approx \{1 + \chi\, C_\infty\}^{-1} \qquad \text{(A10)}$$

where $\chi=F/\varepsilon\varepsilon_0\,(\mu_e\tau_e)$. Therefore, the apparent reduction in the electric field effect for the secondary ions is a function of two parameters: (i) the concentration C_∞ of the cations by the time the electron is trapped and (ii) the lifetime-mobility product $\mu_e\tau_e$ for these electrons. The latter is known from the conductivity measurements of ref. 4, which gives an estimate of $\chi=1.8\times10^6\ M^{-1}$ for $\rho=0.837\ g/cm^3$ and $T=41^oC$ (at which $\varepsilon\approx1.51$ and $\mu_e\tau_e\approx2.5\times10^{-9}\ cm^2/V$). We conclude that for the cation yield that is typically observed in neat sc CO_2 in our pulse radiolysis experiments, that is 0.2-1 μM, the electron-hole recombination in the bulk would considerably decrease the apparent electric field effect on the cation yield. Such a situation is peculiar to sc CO_2, in which the quasifree electrons have high mobility and relatively long "natural" life time.

A more realistic situation is when the formation rate of the free electrons G(t) is much slower than τ_e^{-1}. In such a case, we let $dE/dt\approx0$, $E\ll I$, and $C\approx I$, thus obtaining

$$dC/dt = G(t)/(1+k_2\tau_e\, C) \qquad \text{(A11)}$$

which gives

$$C + 1/2\ k_2\tau_e\, C^2 = \int_0^t G(t')\ dt' = g(t) \qquad \text{(A12)}$$

or

$$C(t) = \{[1+2k_2\tau_e\, g(t)]^{1/2}-1\}/k_2\tau \qquad \text{(A13)}$$

For $\beta\ll1$, we may assume that $\Delta\ln(g)\approx\beta$ and the time-dependent electric field effect on the cation yield

$$\{\Delta C(t)/C(t)\}/\beta \approx \partial \ln C/\ \partial \ln g \rightarrow\approx \{2 - ([1+2\zeta]^{1/2}-1\}/\zeta)\}^{-1} \qquad \text{(A14)}$$

where $\zeta = k_2\tau_e\, g$. For $\zeta\ll1$, $\{\Delta C/C\}/\beta \approx 1$, for $\zeta\gg1$, $\{\Delta C/C\}/\beta \approx 1/2$. This dependence may be anticipated from eq. (A12): for $\zeta\ll1$, $C \propto g$, whereas for $\zeta\gg1$, $C \propto g^{1/2}$. Experimentally (Fig. 11S(b)), the cation yield increases as $g^{0.61}$, regardless of the dose and pulse duration; this suggests that $\zeta>1$. From eq. (A14), the apparent electric field effect on the cation yield, $\Delta C/C$, systematically decreases in magnitude during the electron beam pulse, eventually reaching 50% of its initial value. The tempo of this decrease is given by the dimensionless parameter $\zeta(t)$.

Finally, let us consider a hypothetical system in which the geminate kinetics for the ions is rapid (i.e., the electric field effect develops "instantaneously") and the ions decay by homogeneous neutralization, $dC/dt=-k_r\, C^2$. If the initial yield of these ions is I_0, then

$$C(t) = I_0\ /(1+k_r t\ I_0) \qquad \text{(A15)}$$

In such a case,

$$[\Delta C(t)/C(t)]/\beta \approx \partial \ln C(t)/\ \partial \ln I_0 \rightarrow= (1+k_r t\ I_0)^{-1} \qquad \text{(A16)}$$

© 2002 American Chemical Society, J. Phys. Chem. A, Shkrob jp021494K, Supporting Info Page 13

i.e., the electric field effect $\Delta C(t)/C(t)$ decreases in exactly the same way as the ion concentration. This behavior follows from eq. (A15): for $k_r t\, I_0 >> 1$, $C(t) \approx (k_r t)^{-1}$ is independent of the initial concentration of ions. Eq. (A16) indicates that the electric field effect for free ions is rapidly destroyed by their homogeneous recombination. As shown below, the same happens in a situation when the geminate recombination of the secondary ions occurs on a time scale comparable to that of their cross recombination.

2S.2. Monte-Carlo simulation of the electron dynamics in an isolated geminate pair.

Consider an isolated geminate electron-hole pair. Suppose that an electron with mobility μ_e is trapped with rate constant τ_e^{-1} to give an anion with mobility $\mu_i << \mu_e$. Since the mobilities of the cation (the hole) and the anion are negligible compared to $\mu_e \sim 10\text{-}100$ cm^2/Vs, we may neglect ion diffusion. In such a case, eq. (A2) is still valid. Let $\Omega(t)$ be the survival probability of the electron-hole pair in the absence of electron trapping. With trapping, the concentration of electrons $e = \Omega(t) \exp(-t/\tau_e)$, and the concentration [i] of anions $[i] = 1/\tau_e \int_0^t d\xi\, \Omega(\xi) \exp(-\xi/\tau_e)$, so the cation concentration

$$c(t) = \Omega(t) \exp(-t/\tau_e) + 1/\tau_e \int_0^t d\xi\, \Omega(\xi) \exp(-\xi/\tau_e) \qquad (A17)$$

and the time-dependent electric field effect $\beta(t,\mathbf{E})$ on the cation yield in field $\mathbf{E}$ is given by

$$\beta(t,\mathbf{E}) = c(t,\mathbf{E})/c(t;\mathbf{E}=0) - 1 \qquad (A18)$$

with an asymptotic value $\beta_\infty(\mathbf{E})$ for $t \to \infty$. Using eq. (A18) it is possible to find $\beta(t,\mathbf{E})$ once the survival probability $\Omega(t)$ is known. The latter is a function of the reduced time t/t_c, where t_c is the Onsager time, $t_c = r_c^2/D_e$, $D_e = (kT/e)\,\mu_e$ is the diffusion coefficient of the quasifree electron, $r_c = e^2/4\pi\varepsilon\varepsilon_0 kT$ is the Onsager radius, kT is the thermal energy. Thus, $\beta_\infty(\mathbf{E})$ is a function of a dimensionless parameter $\eta = \tau_e/t_c = (kT/er_c^2)\,\mu_e\tau_e$. For $\mu_e\tau_e \approx 2.5\times10^{-9}$ cm^2/V and $r_c \approx 35.2$ nm ($\varepsilon \approx 1.51$) we obtain $\eta \approx 5.5$. For $\eta >> 1$, $\beta_\infty(\mathbf{E})$ approaches its theoretical value of $\beta_{th} = e\mathbf{E}r_c/2kT$ obtained in the Onsager's theory for $\beta_{th} << 1$.

To estimate $\beta_\infty(\mathbf{E})$, it is sufficient to find the Laplace transform $W(\tau_e^{-1})$ of the survival probability $\Omega(t)$, since

$$c_\infty = 1/\tau_e \int_0^\infty dt\, \Omega(t) \exp(-t/\tau_e) = \tau_e^{-1}\, W(\tau_e^{-1}). \qquad (A19)$$

For $\eta >> 1$, c_∞ may be estimated in the prescribed diffusion theory of Mozumder. [23] For a geminate pair generated at $|\mathbf{r}| = r_0$ with an angle θ between the radius vector $\mathbf{r}$ connecting the charges and the electric field $\mathbf{E}$

$$c_\infty \approx \Omega_\infty \{\, 1 + \exp[\, -\beta_{th}\, z\, (1-\cos\theta)\,]\, [(\beta_{th}^2 + \eta^{-1})^{1/2} - \beta_{th}]\,\} \qquad (A20)$$

where $z = r_0/r_c$ and the free electron yield Ω_∞ is given by

$$\Omega_\infty \approx \exp\{\, - z^{-1} \exp[\, -\beta_{th}\, z\, (1-\cos\theta)\,]\,\} \qquad (A21)$$

For $\beta_{th} << 1$, the latter expression averaged over angles θ yields

$$\Omega_\infty \approx \exp\,(-r_c/r_0)\,(1+\beta_{th}), \qquad (A22)$$

© 2002 American Chemical Society, J. Phys. Chem. A, Shkrob jp021494K, Supporting Info Page 14

For $\beta_{th}^2 << \eta^{-1} << 1$, the angle-averaged eq. (A20) yields

$$c_\infty \approx \exp(-r_c/r_0)\ \{\ 1 + \eta^{-1/2} + \beta_{th}\,[1-r_0/r_c]\,\eta^{-1/2} + o\,(\beta_{th}^2)\ \} \qquad (A23)$$

which gives

$$\beta(\mathbf{E}) \approx \beta_{th}\,(1 - const\ x\ \eta^{-1/2})\ /\{1 + \eta^{-1/2}\} \qquad (A24)$$

The constant in eq. (A24) is a function of the initial charge distribution $\rho(r_0)$ and the Onsager radius r_c. In the general case (for any η), a numerical simulation of the geminate dynamics is needed.

To find $\Omega(t)$, we used a Monte-Carlo approach used by Shkrob and Sauer. [4] An r^2-Gaussian radial distribution $\rho(r_0)$ of the initial pair separation, r_0, was used:

$$\rho(r_0) = 4\,\pi^{-1/2}\,r_0^2\,b_G^{-3}\exp(-[r_0/b_G]^2) \qquad (A25)$$

(the origin of the coordinate system is chosen to be at the positive charge, the initial angular orientation of the pair is random). The electron is generated at $|\mathbf{r}|=r_0$ using this distribution and then moved by small increments

$$\delta\mathbf{r} = (6\,D_e\,\delta t)^{1/2}\,\mathbf{u} + \mu_e\,\{\mathbf{E} + \mathbf{E}_{loc}(\mathbf{r})\}\,\delta t \qquad (A26a)$$

at regular intervals δt of time ($\delta t << t_c$). In eq. (A26), $\mathbf{u}$ is the random unity vector, $\mathbf{E}$ is the vector of the external electric field and

$$\mathbf{E}_{loc}(\mathbf{r}) = -\,(e/4\pi\varepsilon\varepsilon_0)\,\mathbf{r}/|\mathbf{r}|^3 \qquad (A27)$$

is the Coulomb field of the cation. In dimensionless units of time $\delta t'=\delta t/t_c$ and distance $\mathbf{r}'=\mathbf{r}/r_c$, eq. (A26) is reduced to $\delta\mathbf{r}' = (6\,\delta t')^{1/2}\,\mathbf{u} + \{2\,\beta_{th}\,\mathbf{z} - \mathbf{r}'/|\mathbf{r}'|^3\}\,\delta t'$. The time interval $\delta t'$ is sufficiently small (<<1) so that $|\delta\mathbf{r}'| \approx 10^{-3}$. For $|\mathbf{r}| \le 1$ nm, the pair "recombines" and the diffusion trajectory terminates. Typically, (5-10)x10^5 such trajectories were averaged.

Figure 17S shows the calculation of $\Omega(t;\mathbf{E})$ for $\mathbf{E}=0$ and $\mathbf{E}=25$ kV/cm. In this calculation, $b_G=10$ nm which corresponds to the average pair separation $\langle r_0\rangle \approx 11.3$ nm and the free ion yield $\Omega_\infty(\mathbf{E}=0) \approx 5.6\%$. These parameters were used to simulate electric-field-dependent geminate pair dynamics observed for isolated anthracene$^+$/F^- pairs generated in biphotonic 5 eV laser ionization of dilute anthracene solutions in dense sc CO_2 containing SF_6. [4] In the same figure, the cation kinetics $c(t,\mathbf{E})$ calculated using eq. (A20) for $\eta \approx 5.5$ are shown by bold lines. The time-dependent field effect $\beta(t,\mathbf{E})$ on the cation yield (eq. (A18)) and the field effect β^o on the free electron yield

$$\beta^o(t,\mathbf{E}) = \Omega(t,\mathbf{E})/\Omega(t;\mathbf{E}=0) - 1 \qquad (A28)$$

are also shown in Fig. 17S. It is seen that $\beta^o(t,\mathbf{E})$ does not approach $\beta_{th}(\mathbf{E}) \approx 1.62$ even for $t/t_c \sim 100$. The time dependence of the field effect $\beta(t,\mathbf{E})$ on the cation yield reaches a plateau for $t/\tau_e \sim 3$: by this time, all geminate electrons are trapped as anions, and the electric field acts on the slowly-migrating ions. Thus, further development of the electric field effect is

© 2002 American Chemical Society, J. Phys. Chem. A, Shkrob jp021494K, Supporting Info Page 15

arrested. Fig. 18S(a) shows the dependence of $\beta_\infty(\mathbf{E})$ for $\mathbf{E}$=25 kV/cm as a function of η for several values of b_G. These dependencies can be approximated by

$$\beta_\infty(\mathbf{E}) \approx \beta_\infty^{max} /(1+ (\eta/\alpha)^{-\sigma}), \qquad (A29)$$

where $\beta_\infty^{max} \approx \beta_{th}$ (for $\beta_{th}<<1$), $\alpha\approx5.5$ and $\sigma\approx0.68$. For a given η, the field effect $\beta_\infty(\mathbf{E})$ systematically decreases with b_G (that is, with the free electron yield). This trend is easy to rationalize: as the free ion yield approaches unity, there is little room for further increase of this yield by the electric field. For $b_G\approx10$ nm and $\eta\approx5.5$ (obtained from the conductivity experiments) [4] the actual field effect $\beta_\infty(\mathbf{E})$ is ca. 50% of β_{th}. Increasing b_G from 10 nm to 20 nm (which is equivalent to an increase in $\Omega_\infty(\mathbf{E}=0)$ from 5.6% to 20.3%) reduces $\beta_\infty(\mathbf{E})$ from 0.81 to 0.51 (for $\eta\approx5.5$ and $\mathbf{E}$=25 kV/cm). Since the maximum observed prompt electric field effect is ca. 0.8 (Fig. 11), the thermalization distance b_G must be less than 12 nm (equivalent to $\Omega_\infty(\mathbf{E}=0)$ of 8.4%).

The observed effect is further reduced due to homogeneous cross-recombination of electrons with cations that are produced within the generation pulse (section 2S.1). Note that Eq. (A11) is correct only for $\tau_e^{-1} + k_2 C << t_c^{-1}$. In the general case, eq. (A11) should be replaced by

$$dC/dt = G(t)\, \tau_e^{-1} \int_0^\infty d\xi\, \Omega(\xi) \exp(-[\tau_e^{-1}+ k_2 C]\xi) \qquad (A30)$$

where G(t) is the rate for the primary pair formation (assumed to be much slower than τ_e^{-1} and t_c^{-1}). Integration of eq. (A30) yields

$$g/C_{cr} = \int_0^{C/C_{cr}} dx\, \{\eta^{-1}\, w(\eta^{-1} + x)\}^{-1} \qquad (A31)$$

where $\eta = \tau_e/t_c$, $g(t)$ is the integral of G(t), the concentration C_{cr} is given by

$$C_{cr} = 1/k_2 t_c \approx (4\pi N_{av} r_c^3)^{-1}, \qquad (A32)$$

and $w()$ is the dimensionless Laplace transform of $\Omega(t)$ with the time given in the units of t_c. Using the Monte-Carlo calculation for $\Omega(t)$ at $\mathbf{E}$=0 and $\mathbf{E}$=25 kV/cm, we calculated the Laplace transform $w()$ for b_G=10 nm and performed the integration in eq. (A31) for $\eta\approx5.5$. This gives the cation concentration C/C_{cr} as a function of g/C_{cr} (Fig. 19S). The observed field effect $\chi(t)$ is defined as $C(t,\mathbf{E})/C(t;\mathbf{E}=0) - 1$. It is seen from Fig. 19S that for $C>>C_{cr}$, $\chi(t)$ approaches zero: due to efficient cross-recombination with cations formed within the duration of the electron beam pulse, the electron life time becomes shorter than t_c, and the field effect does not develop.

For $r_c\approx35.2$nm, $C_{cr}\approx3.02$ μM. The concentration of $(CO_2)_n^+$ cations formed at zero electric field by the end of the "10 ns", 60 Gy electron pulse used in our experiments corresponds to $C/C_{cr}\approx0.5$. Using the plots in Fig. 11, this yield corresponds to $g(t)/C_{cr} \approx 13$ and the expected field effect on the cation yield is ≈ 0.36. This is ca. 44% of the electric field effect for $C<<C_{cr}$, which is 0.81 (section 2S.1 and Figs. 17S and 18S(a)). The observed drop in the field effect within the duration of the electron pulse is close to 40-50%. As shown in Fig. 11, the calculation fully explains the observed field effect and cation formation kinetics during the electron beam pulse. It also accounts for the decrease in the observed end-of-pulse field effect with the dose (that is, C/C_{cr}) for electron pulses of

© 2002 American Chemical Society, J. Phys. Chem. A, Shkrob jp021494K, Supporting Info Page 16

equal duration (see Fig. 15S(a)). Note that due to the recombination losses, the eventual cation yield per pair, C/g, is much lower than c_∞ given by eq. (A19) (i.e., this formula applies only for $C<<C_{cr}$). For $C\approx1.5$ μM and $\mathbf{E}=0$ (for $\eta\approx5.46$ and $b_G=10$ nm), this yield is 4 % whereas $c_\infty\approx8.4\%$.

The same Monte-Carlo calculation can be used to estimate the effect of the electron scavenger, SF_6, on the cation yield. We can safely neglect both the geminate and cross recombination of the secondary ions during the "10 ns" electron pulse (Fig. 11S(a), trace (ii)) since for these secondary pairs, $t_c \approx 78$ ns. With this assumption, by analogy with eq. (A19) we obtain that in the presence of SF_6, $c_\infty=\tau'^{-1}\, W(\tau'^{-1})$, where $\tau'=\tau_e/(1+\alpha_e[SF_6])$ is the reaction-limited electron lifetime and $\alpha_e=k_{sc}\tau_e$ is the product of the "natural" lifetime τ_e and the electron scavenging rate k_{sc}. In this derivation, the cross-recombination of electrons with cations is neglected since the shortening of the electron lifetime due to reaction with SF_6 far outweighs shortening of this lifetime due to recombination with the cations:

For a given electron scavenger, the product α_e can be obtained from dc photoconductivity measurements for isolated electron-cation pairs (see ref. 4 for data on SF_6, O_2, and CCl_4). Using the estimates of $\eta=\tau_e/t_c\approx5.5$ and $\alpha_e=6.7\text{x}10^3$ M^{-1} obtained in ref. 4, we find that for $[SF_6]=0.02$ M, $\alpha_e[SF_6]\approx130$ and the dimensionless parameter $\eta'=\tau'/t_c\approx0.04$. At this concentration of SF_6, the cation yield at the end of the pulse is $C\approx7.2$ μM (Fig. 4(b)), which gives $k_2\tau_eC = \eta\, C/C_{cr} \approx 13$. The latter parameter is ten times less than $\alpha_e[SF_6]$. For $[SF_6] = 10^{-3}$ M, $\alpha_e[SF_6]\approx6.7$ and $k_2\tau_eC \approx 0.66$ (for $C\approx2$ μM, Fig. 4(b)). Thus, except for $[SF_6]=0$, $\alpha_e[SF_6] >> k_2\tau_eC$ for all concentrations of SF_6 given in Fig. 4(b), and the observed cation yield is proportional to c_∞ given by eq. (A19) with τ_e replaced by τ_e'.

To estimate c_∞, one needs to know the behavior of $c_\infty(\eta')$ for $\eta'<<1$. Most formulas given in the literature do not apply for $\eta'<1$. For example, in the prescribed diffusion treatment of Mozumder, [23] $c_\infty(\eta')/\Omega_\infty \approx 1 + \eta'^{-1/2}$ for $\eta'>>1$. The WAS expression, [20] $c_\infty(\eta')/\Omega_\infty \approx 1 + \eta'^{-0.6}$ applies for $\eta'>0.3$ only. For $\eta'>0.01$, the following empirical formula for $c_\infty(\eta')$ was used (Fig. 18S(b)):

$$c_\infty(\eta')/\Omega_\infty \approx 1 + a\, b\, \{1 - \exp(-\eta'^{-0.6}/b)\} \qquad \text{(A33)}$$

where a and b are the constants dependent of the initial charge distribution. For $\mathbf{E}=0$ and $b_G\approx10$ nm, $a\approx1.3$ and $b\approx9.5$. Fig. 4(b) shows the experimental dependence of the initial cation yield compared to the one obtained using eq. (A30) with fixed parameters $\eta=5.46$ and $\alpha_e=6.7\text{x}10$ M^{-1}. The agreement between the theoretical and experimental dependencies is very good.

2S.3. Cross recombination via a lattice Monte-Carlo simulation.

In concentrated SF_6 solution, the lifetime of the quasifree electrons is very short ($\tau_e'/t_c <<1$), and no electric field effect is developed in the primary pairs. Thus, if the concentration of ions is low, the kinetics of the electric field effect $\beta^o(t,\mathbf{E})$ follow that of $\beta^o(t,\mathbf{E})$. In sc CO_2 at 41°C and $\rho\approx0.85$ g/cm^3, the mobilities of positive and negative solute ions are $2\text{x}10^{-3}$ and $4\text{x}10^{-3}$ cm^2/Vs, respectively. [4,5] For these mobilities, the Onsager time t_c of the geminate (secondary) ion pair is $t_c\approx78$ ns and the Debye constant of homogeneous ion neutralization $k_2\approx4.4\text{x}10^{12}$ M^{-1} s^{-1}. As seen from Fig. 13(b), the

© 2002 American Chemical Society, J. Phys. Chem. A, Shkrob jp021494K, Supporting Info Page 17

experimental kinetics of the electric field effect in the SF_6 solution saturate at 100 ns. For $\mathcal{E}$=25 kV/cm, the maximum field effect is ca. 0.2, which is well below $\beta_{th} \approx 1.62$.

This behavior is caused by cross-recombination of the *ions*. As shown above, such recombination tends to negate the electric field effect on a time scale of $(k_2[C])^{-1}$. As shown in section 3.1, in the concentrated SF_6 solution the extrapolated initial concentration C_0 of the solvent radical cations is 5-10 μM, which corresponds to a half life time of 25-47 ns. These estimates suggest that the development of the electric field effect in the geminate ion pairs and the reduction of this effect due to recombination in random pairs occur on the same time scale. Though there are several analytical treatments for modeling such a situation (e.g., the cylindrical spur model by Jaffe), [21] all of these models use simplifying assumptions that poorly relate to our experimental situation. Therefore, we used a multipair lattice Monte-Carlo simulation that, in essence, is a simplified version of the molecular dynamics models that are commonly used for simulation of ionic liquids: [1S]

At t=0, N cations were randomly placed inside a cubic box with a side length of $L \approx 10\ r_c$. The anions were randomly placed around these cations using the r_0 distribution given by eq. (A18). Periodic boundary conditions were implemented, and the anions were incrementally moved (with $\delta t \approx 20$ ps) using the equation similar to eq. (A19) in which $\mathcal{E}_{loc}$ was the electric field exerted on a given anion by other ions. Typically, only ions in the minimal cell were taken into account, i.e., the difference of Cartesian coordinates r_i^α and r_j^α (α=x,y,z) for the i-th anion and the j-th charge obeyed the condition $-L/2 < r_i^\alpha - r_j^\alpha < L/2$. This minimal cell can be represented by a unit box (0,0,0) centered at the anion. Eight more unit boxes with centers at (i_xL,i_yL,i_zL), i_α=0,±1, form the first layer around this minimal cell. Other layers may be constructed in a similar fashion. In the molecular dynamics models of ionic liquids, Coulomb interactions between the charges in the minimal cell and the charges in the layers around this cell are commonly treated using Ewald summation of the Fourier series (e.g., see Heyes). [2S] For our system, this summation is not needed if the unit box is sufficiently large. Indeed, the charges are efficiently screened from each other. In the Debye-Hückel theory, [3S] the effective potential $V(r)$ between the counter ions decays as $V(r)/kT=(r_c/r)\exp(-\kappa r)$, where the screening radius $\kappa^{-1} = \{8\pi\ r_c\ C\}^{1/2}$. For $C \approx 5$ μM, κ^{-1}=19.5 nm. Thus, the charges that occupy neighboring cells (L≈350 nm) weakly interact with each other. To demonstrate this point, we performed test calculations in which the Ewald summation was extended to 1-3 layers around the minimal cell. No difference was observed between these simulations and the minimal cell simulations, even for the lowest ion concentration (1 pair per a 350 nm box corresponds to 39 nM).

Fig. 20S shows the survival probabilities $c(t,\mathcal{E})$ of the ions calculated for an isolated (single) pair (dashed lines), and for a system containing 1 to 625 pairs per an L=350 nm unit cell (125 pairs per unit cell corresponds to the initial ion concentration of 4.8 μM at t=0). The kinetic traces were calculated for $\mathcal{E}$=0 and $\mathcal{E}$=25 kV/cm. As the concentration increases, cross-recombination becomes more prominent (Fig. 20S(b)). The electric field effect $\beta(t,\mathcal{E})$ first increases in the same fashion as $\beta^o(t,\mathcal{E})$ for an isolated pair (before the onset of the cross-recombination) and then decreases (as the cross-recombination starts to occur). For an initial concentration of 4.8 μM, the maximum effect of 0.4 is attained at 120 ns (Fig. 20S(a)). At longer delay times the field effect slowly decreases. The higher is the initial ion concentration, the lower is the maximum field effect attained. In a more realistic simulation, the unit cell is filled by the ion pairs following the experimental generation function G(t). For the "10 ns" pulse, $G(t) \propto \exp(-[t/t_p]^2)$, where t_p

© 2002 American Chemical Society, J. Phys. Chem. A, Shkrob jp021494K, Supporting Info Page 18

≈ 4.4 ns. Using this pulse profile, we were able to simulate both the observed cation dynamics and the field effect dynamics (Fig. 21S) assuming that the total yield of ion pairs was 26.3 μM per a 59.3 Gy pulse, or 5.1 ion pairs per 100 eV. Typically, the ionization yield is 4-5 pairs per 100 eV, so this estimate is reasonable. In the calculation shown in Fig. 21S(b), a "natural" lifetime of 100 ns was assumed for the solvent radical cation.

Without SF_6, the modeling is more involved, because both the primary and the secondary pair dynamics must be taken into account. In neat sc CO_2, the end-of-pulse yield of the solvent radical cations is 5-6 times lower than in the concentrated SF_6 solutions since in the neat solvent, a large fraction of the primary pairs recombines, geminately and in the bulk. Also, the mobility of $(CO_2)_n^-$ is higher than that of F^-. From the conductivity measurements, the sum of the ion mobilities μ_i is 0.016 cm^2/Vs for the pair involving $(CO_2)_n^-$ vs. $\mu_i=6x10^{-3}$ cm^2/Vs for the pair involving F^- , [4] so that the Onsager time t_c for the former pair is ≈ 30 ns. [4]

To model the kinetics in neat sc CO_2, the same Monte-Carlo program was used, and the electron (with mobility μ_e) was assumed to yield the solvent anion with rate constant of τ_e^{-1}. As seen from the previous discussion, the cation yields do not depend on the exact value of μ_e and τ_e, rather they depend on the product $\mu_e\tau_e$. For certainty, we assumed τ_e=256 ps and μ_e=10 cm^2/Vs, so that τ_e/t_c≈5.47 (where t_c is the Onsager time for the primary electron-hole pair). The electron-hole pairs were generated at the same rate G(t) as in the calculation for the SF_6 solution. When the electrons were present in the unit cell, the time increment δt was 6 fs; when only ions were in the unit cell, δt was increased to 3.8 ps.

Fig. 22S(b) shows the cation yield and the kinetics of the electric field effect on the cation yield plotted against the total yield of the electron-hole pairs (for the t_p=4.4 ns, 59.3 Gy generation pulse). One set of data shown in Fig. 22S(b) was obtained using the lattice Monte-Carlo calculation as discussed above (symbols), another was obtained using the semianalytical treatment of section 2S.2, eq. (A31) (lines). The two calculations agree well except for higher concentrations (near the end of the "10 ns" generation pulse, trace (v) in Fig. 22S(a)). This divergence is caused by the recombination of the secondary pairs that is neglected in the semianalytical treatment. The main difference is in the field effect kinetics: the lattice model yields a lower estimate for the field effect at the start of the generation pulse. A comparison with the experimental field effect kinetics shown in Fig. 11 demonstrates that both the lattice Monte-Carlo and the semiempirical calculations give satisfactory fit of the experimental data.

Fig. 22S(a) shows a calculation in which 12% of the pairs were assumed to involve the CO_3^- anion instead of the quasifree electron (the same distribution of thermalization distances was assumed). We assumed the same mobility for CO_3^- and CO_4^- anions. At this initial fraction of the CO_3^- anions, the end-of-pulse yield of the solvent radical cation increases by 40% (traces (iii)) as compared to this yield in a calculation without the CO_3^- anions (traces (ii) and (iv)) in Fig. 22S(a)), whereas the initial field effect decreases by two times (traces . Both the increase in the yield and decrease in the field effect stem from the slow charge separation dynamics in the pairs that involve the CO_3^- radical: the survival probability at 5-10 ns is large and $t/t_c<<1$, so that the prompt field effect in such pairs is small. Eventually, the field effect in such pairs starts to increase. In the calculation shown in Fig. 22S(a), trace (iv), this increase occurs between 10 and 30 ns. At later delay times, the cross recombination arrests this increase, and the field effect starts to decrease with time. For small initial fractions of CO_3^- anions (< 15%), the increase in the cation yield and the decrease in the initial field effect are proportional to the fraction. We found that to agree

© 2002 American Chemical Society, J. Phys. Chem. A, Shkrob jp021494K, Supporting Info Page 19

with the experimental kinetics and dose dependencies shown in Figs. 11, 11S(b), and 34S(a), the initial fraction of the CO_2 anions cannot exceed 2-3%.

3S. Scavenging experiments with O_2, N_2O, and CO.

It is known that the solvent radical anion in sc CO_2 does not react with N_2O and CO. [4] By contrast, all three solutes rapidly react with the solvent hole (Table 1). [1,2] As shown below, the end product of the scavenging reaction is the dimer (or multimer) radical cation of the solute.

N_2O. The ionization potential of N_2O is 0.88 eV lower than CO_2 (Table 1). [53] In the gas phase, $(CO_2)_2^+$ reacts with N_2O to yield a metastable $(N_2O.CO_2)^+$ cation; the latter rapidly reacts with another N_2O molecule to yield an $(N_2O)_2^+$ dimer cation. [4S] In sc CO_2, the solvent radical cation reacts with N_2O with rate constant of 4.1×10^{10} M^{-1} s^{-1} which is close to 3.9×10^{10} M^{-1} s^{-1} for O_2 (Table 1). Judging from these large rate constants, the reaction is a charge transfer.

When 0.1-1 M of N_2O is added to the radiolysate, the solvent radical cation reacts with N_2O within the duration of the electron pulse, and a new absorption band, centered at 650 nm, emerges (Fig. 39S). This 650 nm band is superimposed on the "tail" absorbance from the solvent radical anion whose yield is not changed by addition of N_2O. The same 650 nm band is observed at lower concentrations of N_2O (0.3-10 mM). For these concentrations, the formation of the 650 nm band occurs on the same time scale as the decay of the 750 nm band from the solvent hole (Figs. 30S(a) and 39S). Due to the short "natural" life time of the solvent hole, relatively high concentration of N_2O (> 0.1 mM) must be added to observe hole scavenging on the time scale of the experiment. Since diffusion-controlled reactions in sc CO_2 have rate constants ~ 10^{11} M^{-1} s^{-1}, [1,2,4] assuming that the resulting $(N_2O.CO_2)^+$ cation can dimerize with another N_2O molecule, the formation of the the $(N_2O)_2^+$ dimer would occur on the same time scale as the decay of the solvent radical cation. As shown in Part II of this series, [10] the $(N_2O.CO_2)^+$ cation does not absorb in the visible whereas the $(N_2O)_2^+$ dimer cation does. It appears that the dimerization of $(N_2O.CO_2)^+$ occurs at least as fast as the initial charge transfer.

We argue that the 650 nm band is from the $(N_2O)_2^+$ dimer cation. [10,51] The latter has structure and energetics similar to those of the $(CO_2)_2^+$ dimer cation, [10,48,51] as these two species are isoelectronic. A similarity between the 650 nm band of $(N_2O)_2^+$ and the 750 nm band of solvent radical cation supports our assertion that $(CO_2)_2^+$ constitutes the chromophore core of this solvent radical cation. [1,2]

Oxygen. From the photoconductivity studies of Shkrob and Sauer, [4] it is known that $(CO_2)_n^-$ reacts with O_2 with rate constant of 8×10^9 M^{-1} s^{-1} to yield CO_4^-. O_2 also reacts with e_{qf}^-, and the electron life time decreases with $[O_2]$ as $(1+\alpha_e[O_2])^{-1}$, where $\alpha_e \approx 580 \pm 130$ M^{-1}. When 5 mM O_2 is added to the solution (as in the experiments of Takahashi et al.), [3] 74% of the electrons are promptly scavenged by O_2 and the life times of the solvent radical anion and the solvent radical cation are reduced to 25 ns and 5 ns, respectively (Figs. 29S and 40S). Consequently, the transient spectra observed in the oxygenated solutions are dominated by the absorbances from the solute ions and (at later delay times) by the 550 nm band of the neutral product.

© 2002 American Chemical Society, J. Phys. Chem. A, Shkrob jp021494k, Supporting Info Page 20

The absorption spectrum of CO_4^- is not known. IR spectroscopy studies of the matrix-isolated CO_4^- anion indicate that this species is bleached by the UV light only. [5S] In the photoconductivity study of Shkrob and Sauer, [4] no electron detachment upon 532 nm photoexcitation of CO_4^- in sc CO_2 was observed, which suggests that this species does not absorb in the visible. By contrast, the gas-phase CO_4^+ cation has weak optical absorbance in the visible due to electron transfer from the CO_2 to the O_2 moiety. [6S] The photodestruction spectrum of CO_4^+ has an onset at 620 nm and a peak at 530 nm. [6S] CO_4^+ binds to several more CO_2 molecules to yield $O_2^+(CO_2)_n$ cations; [4S] photodissociation spectra of these cations are not known. At higher O_2 pressure, CO_4^+ reversibly reacts with O_2 to yield the O_4^+ dimer cation. [6S] The latter cation also absorbs in the visible and exhibits similarly low cross section for photodissociation ($< 2x10^{-18}$ cm^2). [6S]

Figs. 27S, 40S, and 41S shows typical kinetics and transient absorption spectra observed in the oxygenated solutions. Addition of > 10 mM O_2 completely eliminates the prompt ΔOD_λ signals from the solvent radical ions (Fig. 41S). The spectra obtained at the end of the pulse are dominated by a "tail" (λ<500 nm) of a UV band (Fig. 41S(b)). This absorbance decays on the same time scale as the solvent radical anion in neat sc CO_2 (Fig. 40S(a) and λ<550 nm traces in Fig. 27S). Part of this absorbance can be removed by addition of 1-3 M of H_2 (not shown). This suggests that the λ<500 nm band is composite. Some of the VIS absorbance could be from the CO_4^+ or O_4^+ cations; most of it should be from the CO_4^- anion. More work is needed to decompose this complicated spectrum.

After the first 500 ns, the oxygen ions are gone and the VIS spectrum is dominated by the 550 nm band of the neutral product (Fig. 41S(b)). Since these ions do not absorb at λ>500 nm, the formation kinetics of this neutral product (with a time constant of ca. 100 ns) can be clearly observed for λ>550 nm (Fig. 27S, 40S(c), and 41S(a)). Remarkably, these kinetics and the yield of the neutral product do not change with [O_2] (compare 4 mM, 19 mM, and 0.42 M kinetics in Fig. 41S(c)), i.e., the precursor of the neutral product does not react with O_2. Note that the decay kinetics obtained at 400 nm do not change with [O_2] (Fig. 40S(a)); this wavelength must be an isosbestic point for the solvent and oxygen ions.

CO. In the gas phase, $(CO_2)_2^+$ reacts with CO forming the $(CO_2.CO)^+$ cation; the latter reacts with another CO molecule forming a $(CO)_2^+$ cation (rate constants for both of these reactions are similar). [4S,7S] In high-pressure CO_2:CO mixtures, further polymerization occurs, and the trimer and higher multimer cations are formed. [8S] The $(CO_2.CO)^+$ cation is unlikely to absorb in the visible, but the situation with the $(CO)_2^+$ cation is not clear. In the gas phase, this cation does not absorb in the visible (the photodestruction cross section is $< 10^{-19}$ cm^2). [6S,9S] On the other hand, it was found that the IR [10S] and EPR [11S] signals from the *trans*-$OCCO^+$ cations in solid neon can be bleached with $\lambda < 560$ nm light. Thompson and Jacox [10S] explain this bleaching by recombination of the dimer cation with electrons that are photodetached from the *trans*-$OCCO^-$ anions present in the same matrix.

Transient absorbance kinetics obtained for sc CO_2 solutions of CO are difficult to interpret since several species contribute to the UV-VIS absorbance. The easiest to interpret are the kinetics obtained for λ>650 nm (Fig. 42S), as these are the same as the kinetics for the product formation that are observed in the same spectral region in the O_2 and H_2 solutions (Fig. 42S(b)). These kinetics do not change when 8-25 mM of O_2 is added to the CO solution (Fig. 42S). The spectra observed after the first 500 ns are those of the neutral

© 2002 American Chemical Society, J. Phys. Chem. A, Shkrob jp021494K, Supporting Info Page 21

product. Addition of CO (to 0.2 M) does not change the product yield and the formation kinetics.

When 1-7 mM of CO is added, faster decay of the solvent hole at 900 nm is observed (Fig. 28S), yielding a rate constant which is 3.13 times lower than that for N_2O (Table 1). This agrees with the gas phase data, as $(CO_2)_2^+$ reacts with CO three times slower than with N_2O. More surprising is the formation of a new absorption band at 550-650 nm (Fig. 43S). The formation kinetics for this band is delayed, by tens of nanoseconds, relative to the decay kinetics of $(CO_2)_n^+$ observed at 900 nm (Fig. 28S). This new band is more prominent in concentrated CO solutions (0.24 M), but it is also seen at lower concentrations (7 mM); see Fig. 43S. For [CO]≈0.24 M, the increase in the 550-650 absorbance is 2.5 times faster than the increase in the 700-800 nm absorbance from the neutral product. The 550-650 nm band is not formed when the solvent hole is scavenged by O_2 and H_2 (Fig. 43S) Therefore, this band is from a solute cation.

Given that the $(CO)_2^+$ cation does not absorb light in the visible, [9S,10S] it seems that the delayed formation of the 550-650 nm absorbance cannot be accounted for by the formation of this dimer cation. We suggest that this band originates from a higher $(CO)_n^+$ multimer.

4S. Additional References (Supporting Information).

1S. Allen, M. P.; Tildesley, D. J. *Computer Simulation of Liquids*; Clarendon Press: Oxford, 1993.

2S. Heyes, D. M. *J. Chem. Phys.* **1981**, *74*, 1924.

3S. Atkins, P. W. *Physical Chemistry*; W. H. Freeman & Co.: San Francisco, 1978; Ch. 11.2.

4S. Sieck, L. W. *Int. J. Chem. Kinet.* **1978**, *10*, 335.

5S. Jacox, M. E.; Thompson, W. E. *J. Phys. Chem.* **1991**, *95*, 2781.

6S. Smith, G. P.; Lee, L. C. *J. Chem. Phys.* **1978**, *69*, 5393; 45; Smith, G. P.; Lee, L. C.; Moseley, J. T. *J. Chem. Phys.* **1977**, *67*, 3818.

7S. Van Koppen, P. A. M.; Derai, R.; Kemper, P.; Liu, S.; Bowers, M. T. *Int. J. Mass Spectr. Ion Proc.* **1986**, *73*, 41

8S. Norwood, K.; Guo, J.-H.; Luo, G.; Ng, C. Y. *J. Chem. Phys.* **1989**, *90*, 6026

9S. Blair, J. T.; Weisshaar, J. C.; Carpenter, J. E.; Weinhold, F. J. Chem. Phys. **1987**, *87*, 392

10S. Thompson, W. E.; Jacox, M. E. *J. Chem. Phys.* **1991**, *95*, 735.

11S. Knight, Jr., L. B.; Steadman, J.; Miller, P. K.; Bowman, D. E.; Davidson, E. R.; Feller, D. *J. Chem. Phys.* **1984**, *80*, 4593.

© 2002 American Chemical Society, J. Phys. Chem. A, Shkrob jp021494K, Supporting Info Page 22

5S. Figure Captions (Supporting Information).

Fig. 1S.

Front view of cell-1. On the left side, two NPT 1/16" ports and a thermocouple port are indicated. On the top, SHV is a high-voltage connector.

Fig. 2S.

Midsection of cell-2.

Fig. 3S.

A sketch of cell-2 that was used for static experiments. A steel window pusher is drawn separately (bottom right corner). Same cell was used in experiments reported in refs. 1 to 3.

Fig. 4S.

Electrical and optical layout of the experiment. CC is the ceramic cell, HVPS is the 5 kV power supply, RB is the relay box, COMP is the computer, EB is the electron beam from the linac, M1 and M2 are aluminum mirrors, SH is the computer-controlled Uniblitz model VS25S2ZMO light shutter (Vincent Associates), XeL is the Xe arc lamp, FO is the focusing optics, FW is the interference filter wheel, PD is the fast photodiode, and DSO is the digital sampling oscilloscope.

Fig. 5S.

Layout of the high-pressure system. PV is the pressure vessel, CB is a cryogenic bath, HE is a heat exchanger, PU is a JASCO model PU-980 HPLC pump , PT is a Cole-Parmer model K1, 3000 psi pressure transducer, POD is an SSI LO-Pulse pump oscillation damper, PH is a pre-heater pipe, WB is a water bath with a circulating pump, TC1 and TC2 are temperature controllers, INJ1 is a Rheodyne 7725 high-pressure injector with a 5 μL loop (used to inject liquid solutes), INJ2 is a Rheodyne 7010 high-pressure injector with 20 or 200 μL loops (used to inject gaseous solutes), SV is a six-port Rheodyne 7000 stream switching valve with dead volume of 7 μL. Three ports of the SV are used, respectively, for rinsing the system with organic solvent, venting the gases, and filling, purging, or drying the system with a gas mixture (GM); two other ports are blocked. V1 is an SSI model 02-0120 low-volume shut-off valve, GV1 to GV3 are low-pressure Bellow valves (NUPRO SS-2H), RV is a NUPRO model R3A proportional relief valve. The temperature of the pressure vessel is regulated using four 10 W cartridge heaters (Omega model CIR 1014/120) and an air-blowing fan.

Fig. 6S.

Layout of the high-pressure system used for flowing sc CO_2 solutions of SF_6 and H_2 (sections 3.2 and 1S.3). The same equipment as in Fig. 5S was used. PT1 and PT2 are pressure transducers, SB is a Swagelock model 316L-50DF4-500 steel bottle with the inner volume of 500 cm^3, TC3 is a proportional temperature controller, V2 is a diaphragm valve (NUPRO SS DSS4). The operation of this system is explained in section 1S.3.

© 2002 American Chemical Society, J. Phys. Chem. A, Shkrob jp021494K, Supporting Info Page 23

Fig. 7S.

(a) Optical density ΔOD_{633} of a 1.2 mm thick borosilicate plate scanned along the z-axis of cell-2 (see Fig. 8S) using a 5mm x 50 μm beam from a laser diode module. The plates were irradiated using thirty 120 nC, "20 ns" pulses of 20 MeV electrons from the Argonne linac. No beam collimator was used to obtain these traces. The plates were positioned in the yz plane. Trace (ii) was obtained in air; trace (i) was obtained for the glass plate squeezed between two half-cylinders made of nylon that fit inside cell-2. The electron beam passed through a 10 mm thick Suprasil window before entering the cell. (b) Relative doses in cell-2 with (ii) and (i) without a steel collimator (an 8 mm thick aperture with a 2 mm x 5 mm rectangular cutout, see Figs. 1S and 8S). The solid bold lines are normalized ΔOD_{633} traces obtained by scanning the glass plates in the direction of the electron beam (axis z) at the cell midsection. Thin lines are relative doses obtained by averaging the distribution in the xy plane using eq. (1S) with the parameters obtained in Fig. 8S.

Fig. 8S.

(a,b) Normalized ΔOD_{633} traces as a function of the vertical (x) and horizontal (y) displacement relative to the cell axis (for cell-2 without the electron beam collimator). Several traces obtained for different depths z are juxtaposed. It is seen that the dose distribution in the horizontal plane does not change with z. The traces were fit with Gaussian functions, and the dispersion parameter σ_x plotted as a function of z in (c). This parameter linearly increases with z (by 0.25 mm/mm) suggesting that the beam diverges by 14.4° in the xz plane. The same divergence was obtained with the beam collimator (see section 1S.2 for the values of σ_x and σ_y).

Fig. 9S.

(a) Relative dose distribution along the cell axis z for (i) cell-1 (L=2.64 cm) and (ii) cell-2 (L=5 cm, no beam collimator), in air. (b) Effect of inhomogeneous dose deposition on the dependence of *average* cation yield $\langle C \rangle$ on *average* $\langle g \rangle$. Trace (i) is theoretical C vs. g dependence obtained in section 2S.2 (trace (i) in Fig. 19S). Traces (ii) and (iii) are obtained by averaging trace (i) across the cell using the dose distributions given in Fig. 9S(a), as explained in section 1S.2.

Fig. 10S.

(a) The typical λ=500 nm transient absorption kinetics from oxygen-saturated 10 mM solution of KSCN in nanopure water in cell-2 (no beam collimator; optical path L=5 cm). For t>1 μs, the absorbance is from the $SCN^{\bullet -}$ radical anion; the initial "spike" is from hydrated electrons that are rapidly scavenged by oxygen. The pulse charge was (from bottom to top) 30, 70, and 122 nC (for the electron pulses with nominal length of 4, 10, and 20 ns respectively). The time profiles of these pulses are shown in Fig. 11S(a). Dashed lines are biexponential fits of the decay kinetics. Extrapolation of these kinetics to t=0 yields the "initial" yield of $SCN^{\bullet -}$ (b) Extrapolated optical absorption of $SCN^{\bullet -}$ as a function of the pulse charge, for pulses of different duration. The initial (linear) part of this plot gives a slope equivalent to 0.81 Gy/nC.

© 2002 American Chemical Society, J. Phys. Chem. A, Shkrob jp021494K, Supporting Info Page 24

Fig. 11S.

(a) Time profile of 600 nm Cerenkov light produced as the electron beam passes through cell-1 filled with sc CO_2. Nominal pulse length is (i) 4 ns, (ii) 10 ns, and (iii) 20 ns. Traces (i) and (ii) can be fit with Gaussian curves; the corresponding fwhm's are 5 and 7.6 ns, respectively. (b) Juxtaposition of the experimental $\langle C \rangle$ vs. $\langle g \rangle$ dependencies for solvent radical cations generated in pulse radiolysis of neat sc CO_2. Average cation yield $\langle C \rangle$ was found from the 900 nm absorbance kinetics using the known extinction coefficient (section 3.1), and average $\langle g \rangle$ was found using integrated traces in Fig. 11S(a) that were scaled by the average total dose determined using an aqueous thiocyanate dosimeter (e.g., Fig. 10S). We assumed the yield of 5 electron-hole pairs per 100 eV of absorbed radiation (and assumed that the stopping power of the sample scales with the solvent density). The data for cell-1 (with the beam collimator) and cell-2 (without the collimator) are shown on the same plot (see the legend in the plot), for 4, 10, and 20 ns pulses. The cation concentrations obtained for cell-1 are multiplied by 1.25, to facilitate the comparison. The solid line is the $\langle C \rangle = \alpha \langle g \rangle^{\sigma}$ dependence with σ=0.61. While the proportionality coefficient α varies between the cells and the experimental conditions, the power dependence does not change.

Fig. 12S.

As in Fig. 11S(b). Three sets of data are plotted together: for cell-2 with the electron beam collimator, for cell-2 without the collimator, and for cell-1 with the collimator (see the legend in the plot). The solid line is the theoretical C vs. *g* dependence for an infinitely thin radiolytic cell (section 2S.2 and Fig. 19S, trace (i)). This figure illustrates the extent of variation in the $\langle C \rangle$ vs. $\langle g \rangle$ plots with the experimental conditions.

Fig. 13S.

(a) The typical transient absorbance kinetics from 10 mm thick Suprasil windows (cell-2) obtained at *(from bottom to top)* 900, 750, and 550 nm (7.6 ns fwhm, 70 nC pulse). The solid lines are the kinetics obtained when the analyzing light passed through both windows; dotted lines are the kinetics obtained from the front window alone. (b) Typical spectra of window absorbance obtained by integration of the kinetics shown in Fig. 13S(a) between 300 ns and 1 μs *(open squares)*. Filled circles give the spectrum of the stable product in sc CO_2 (window absorption subtracted) obtained under the same conditions. For λ>500 nm, the two spectra are similar; in the UV, these spectra are different.

Fig. 14S.

Evolution of the transient absorbance spectra in neat sc CO_2 (7.6 fwhm, 60 Gy pulse). The time integration windows are indicated in the plot. The data were obtained using a 90° detection scheme (cell-2): the analyzing light was perpendicular to the electron beam. This detection scheme drastically reduces the irradiation of the windows by the electron beam; the 550 nm band from a stable product is still observed.

© 2002 American Chemical Society, J. Phys. Chem. A, Shkrob jp021494K, Supporting Info Page 25

Fig. 15S.

(a) End-of-the pulse electric field effect χ_0 on the yield of 900 nm absorbance in pulse radiolysis of neat sc CO_2 (7.6 ns fwhm pulse, E=25 kV/cm, cell-1). Different points correspond to the pulse charge of *(from right to left)* 17.5, 27.5, 47, and 63.3 nC. The concentration C of the radical cation (found from the corresponding optical density) is given in units of "critical" concentration C_{cr}≈3.02 μM (section 2S.2). The solid line is a theoretical dependence obtained in section 2S.2. (b) End-of-the pulse electric field effect χ_0 as a function of the electric field (7.6 ns fwhm pulse, 70 nC).

Fig. 16S.

(a) Transient absorbance kinetics at 900 nm in radiolysis of neat sc CO_2 (7.8 ns fwhm pulse of 84 nC, a total dose of 67 Gy/pulse, and a repetition rate of 0.3 Hz) as a function of number of pulses absorbed by a static sample (cell-2, no beam collimator). The number of pulses is indicated in Fig. 16S(b). Filled circles indicate the kinetics obtained from the sample flowed at a rate of 2 cm^3/min through the cell (inner volume of 13.4 cm^3) (b) As more radiolytic products are accumulated, the life time k_1^{-1} of the solvent radical cation becomes progressively shorter. The decay constant increases by $2.8x10^5$ s^{-1} per pulse.

Fig. 17S.

To the left axis: time dependencies of the survival probability $\Omega(t)$ for an isolated geminate electron-hole pair *(solid lines)* and the cation concentration c(t), eq. (A17) *(dashed lines).* The upper $\Omega(t)$ and c(t) traces are for E=25 kV/cm, the lower - for E=0. *To the right axis:* The field effects $\beta^o(t,E)$ *(dashed line)* and $\beta(t,E)$ *(filled circles)* on the survival probability $\Omega(t)$ and the cation yield c(t), respectively (eqs. (A28) and (A24), respectively); for E=25 kV/cm. These Monte-Carlo calculations were carried out for t_c=78 ns. Note that the traces plotted as a function of (t/t_c) do not depend on the actual t_c. Cation concentration c(t) was obtained from $\Omega(t)$ for τ_e/t_c=5.46. The initial charge distribution is r^2-Gaussian (eq. (A25)) with b_G=10 nm. This distribution yields an average ion pair separation of 11.3 nm and a free ion yield Ω_∞ = 5.6%.

Fig. 18S.

(a) Dependence of the electric field effect $\beta_\infty(E)$ on the cation yield at $t\to\infty$ as a function of the ratio $\eta=\tau_e/t_c$ (E=25 kV/cm). Several such dependencies for different parameters b_G (eq. (A25) are shown (the values of b_G are indicated in the plot). As the electron-hole separation increases, the electric field effect decreases. For η=5.46, b_G must be ~ 10-12 nm for the initial field effect to be ~ 0.8 (see Fig. 11). (b) *Symbols:* Asymptotic cation yield c_∞ at E=0 as a function of ratio η for several values of the parameter b_G. The solid lines are the least-squares fits obtained using eq. (A33). The 10 nm trace was used to obtain the theoretical curve in Fig. 4(b) (see sections 4.1 and 2S.2) for more detail.

Fig. 19S.

Cation yield, C, for E=0 and E=25 kV/cm (traces (i) and (ii), respectively, *to the left axis*), and time-dependent field effect χ on the cation yield at E=25 kV/cm (trace (iii), *to the right axis*) as a function of the total yield *g* of the electron-hole pairs. The concentration *g* for a given C was determined by solving eq. (A31). The survival probabilities $\Omega(t)$ from the Monte-Carlo calculations shown in Fig. 17S were used in the calculation. We further assumed that τ_e/t_c=5.46. The concentrations are given in units of the "critical" concentration

© 2002 American Chemical Society, J. Phys. Chem. A, Shkrob jp021494k, Supporting Info Page 26

$C_{cr}=(k_2t_c)^{-1}$ (in these units, the plots do not change as a function of the constant k_2 of ion recombination in the bulk). As *g* increases, the field effect decreases. Only for $g<<C_{cr}$ does the field effect approach the theoretical values for an isolated pair that are given in Fig. 18S(a).

Fig. 20S.

(a) *To the left axis: Solid lines:* A lattice Monte-Carlo calculation for the survival probability c(t)/c(t=0) for an ion pair with $t_c\approx78$ ns and $b_G=12$ nm (which corresponds to an average separation of 13.5 nm and $\Omega_\infty\approx8.4\%$). The initial concentration at t=0 is 125 ion pairs in an L=350 nm unit cell, which is equivalent to 4.8 μM. The upper trace is for electric field E=25 kV/cm, the lower trace is for E=0. *Dashed lines:* same for an isolated ion pair. *To the right axis: Filled circles* indicate the field effect $\chi(t)$ for E=25 kV/cm as observed in a c(t=0) = 4.8 μM solution; the dashed line is for an isolated ion pair. The field effect passes through a maximum at 150 ns. At this delay time the effect is just 0.4, which is well below $\beta^o(t\rightarrow\infty)$ for an isolated pair.

(b) *Solid lines:* a family of the field effect kinetics (same parameters as in Fig. 20S(a)) for E=25 kV/cm for several initial ion pair concentrations (the molar concentrations are indicated in the plot). *Dashed line* indicates the field effect kinetic for an isolated ion pair. *Filled circles* indicate the experimental $\chi(t)$ kinetics observed for solvent radical cations in 0.17 M solution of SF_6 in sc CO_2 (Fig. 13(b)). The experimental data are plotted out to 200 ns, though the points obtained for t>80 ns are not reliable (not shown in Fig. 13(b)).

Fig. 21S.

Matching experimental (Fig. 13) and theoretical kinetics for the solvent radical cation, C(t), and the field effect, $\chi(t)$, in 0.17 M solution of SF_6 in sc CO_2. The theoretical model is a lattice Monte-Carlo simulation in which 680 ion pairs are generated in an L=350 nm unit cell following the Gaussian time profile (t_p=4.42 ns) shown in Fig. 11(a), trace (ii). This concentration is equivalent to a total yield of 26.3 μM of the pairs (or 5.1 ion pairs per 100 eV for a 59.3 Gy pulse). In the calculation, it is assumed that quasifree electrons instantaneously attach to SF_6 to produce slowly-migrating fluoride anions. An Onsager time t_c of 78 ns was assumed for the secondary geminate pairs of F^- and $(CO_2)_n^+$ ($\mu_i\approx6\times10^{-3}$ cm/Vs). *To the left axis:* The time profile of the electron pulse is shown as a shaded curve. Dashed lines are experimental kinetics obtained from the ΔOD_{off} and ΔOD_{on} kinetics (E=25 kV/cm) at 900 nm (an extinction coefficient of $\varepsilon^+_{900}=2370$ M^{-1} cm^{-1} was used to obtain the concentrations). Solid lines are lattice Monte-Carlo calculations for E=0 and E=25 kV/cm; these traces were convoluted with an exponential, $\exp(-k_1t)$, to take into account scavenging the solvent radical cation by impurity in sc CO_2 ($k_1^{-1}\approx100$ ns). The deviation of the theoretical kinetics from the experimental ones (20 to 50 ns) is due to a mismatch between the values for ε^+_{900} obtained in the kinetic simulations in Fig. 4(a) and hole-scavenging experiments with *n*-hexadecane (section 3.1): the experimental kinetics are slower than calculated because the dose distribution in the real sample is not uniform (section 2S.2), and the solution at the back of the 2.64 cm long cell-1 absorbs much lower dose that the solution at the cell front (lower initial concentration results in slower second-order decay of the ions by recombination in the bulk). *To the right axis:* The electric field effect $\chi(t)$ for E=25 kV/cm observed at 900 nm (filled circles) and 700 nm (straight crosses) replotted from Fig. 13(b). The solid line is the calculated field effect in the lattice Monte-Carlo model with the parameters given above.

© 2002 American Chemical Society, J. Phys. Chem. A, Shkrob jp021494K, Supporting Info Page 27

Fig. 22S.

(a) A lattice Monte-Carlo calculation for the kinetics of the solvent radical cation in neat sc CO_2. The same electron-hole pair yield of 5.1 per 100 eV was assumed (Fig. 21S), and the τ_e/t_c ratio for the electron-hole pair was 5.46. For the secondary pairs (that involve trapped electrons) $\mu_i \approx 0.016$ cm^2/Vs was assumed (ref. 4). Two calculations are shown. In one calculation (traces (i) and (ii)), the prompt yield of CO_3^- anions was zero. In the second calculation (traces (iii) and (iv)), CO_3^- anions comprised 12% of the total ionization yield (i.e., 12% of the ionization events resulted in the formation of this anion). The same spatial distribution was assumed for the electron-hole and CO_3^--hole pairs. Traces (i) *(solid lines)* and (iii) *(dashed lines)* are the cation kinetics (the upper traces are for E=25 kV/cm, the lower traces are for E=0). Traces (ii) (filled circles) and (iv) (straight crosses) are the field effect kinetics, $\chi(t)$ (for E=25 kV/cm). Trace (v) is the time profile of the generation pulse.

(b) C vs. *g (to the left axis)* and χ vs. *g (to the right axis)* dependencies obtained in the lattice Monte-Carlo calculation (traces (i) and (ii) in Fig. 22S(a)) without CO_3^- anions *(symbols)* and the semianalytical model of section 2S.2 (assuming $C_{cr} \approx 3.02$ μM). Traces (i) and (ii) are the cation concentrations at E=0 and E=25 kV/cm, respectively, and trace (iii) is the field effect, $\chi(t)$. Both models yield similar results.

Fig. 23S.

(a) Scavenging of the solvent radical cation in sc CO_2 by dihydrogen: Transient absorbance kinetics at λ=900 nm in solutions of H_2 in sc CO_2. At this wavelength, the absorbance is from the solvent radical cation alone. The solute concentrations are indicated in the plot. (b) The plot of the pseudo-first-order rate constant k_1 as a function of $[H_2]$. The slope of this linear dependence yields the scavenging constant given in Table 1.

Fig. 24S.

Normalized difference traces obtained by subtraction of the ΔOD_λ kinetics from the 1.66 M solution of H_2 in sc CO_2 from the corresponding kinetics in neat sc CO_2. At this concentration of H_2, the life time of the solvent radical cation is < 8 ns. Since H_2 does not react with the solvent radical anion and the neutral product, the difference kinetics are those of the solvent radical cation alone. This is why these kinetics do not change with the wavelength λ (indicated in the plot), whereas the (composite) kinetics shown in Fig. 2 strongly vary with the detection wavelength.

Fig. 25S.

ΔOD_λ kinetics at (a) λ=500 nm, (b) λ=600 nm, and (c) λ=700 nm obtained in pulse radiolysis of sc CO_2 containing 0, 0.25, 0.62, and 1.66 M of hydrogen (see the color table in the plot). Addition of H_2 shortens the decay kinetics of the solvent radical cation, and the presence of two other light-absorbing species becomes apparent. At 700 nm, the formation of the stable product is clearly observed (see also Fig. 26S). At 500 nm and 600 nm, the signal observed at the high concentration of H_2 is composite: both the solvent radical anion and the neutral product contribute to these kinetics.

Fig. 26S.

Time evolution of the absorbance signals in pulse radiolysis of 1.66 M H_2 in sc CO_2. To facilitate the comparison between the kinetics obtained at different detection wavelengths

© 2002 American Chemical Society, J. Phys. Chem. A, Shkrob jp021494K, Supporting Info Page 28

(see the color table in the plot), the kinetics were normalized at t=0.5 μs. The initial "spike" from the solvent radical cation (that is rapidly scavenged by H_2) is not shown. Both the stable product (whose slow formation kinetics is most clearly seen at 700 nm) and the solvent radical anion (whose decay kinetics is most clearly seen at 450 nm) contribute to the signals in the visible.

Fig. 27S.

A comparison between the transient absorbance kinetics (450 to 700 ns) obtained in 1.66 M solution of H_2 and 0.42 M solution of O_2. CO_4^- contributes to the absorbance signal at $\lambda<500$ in the latter solution; for $\lambda>500$ nm, the signal is mainly from the stable product. The initial "spike" in the kinetics from the hydrogen solution is from the solvent radical cation (that is rapidly scavenged by H_2). For clarity, the kinetics obtained at different wavelengths are stacked on top of each other.

Fig. 28S.

Same as Fig. 23S, for carbon monoxide.

Fig. 29S.

Same as Fig. 23S, for oxygen. Solid lines drawn through the kinetic traces are single-exponential fits.

Fig. 30S.

Same as Fig. 23S, for nitrous oxide. Note the biexponential decay kinetics for 3.5 and 7.6 mM traces in Fig. 30S(a). This is due to the formation of light-absorbing $(N_2O)_2^+$ dimer radical cation (see Fig. 39S and section 3S). At $[N_2O]=0.174$ M, the formation of this dimer cation is instantaneous on the time scale of the experiment. The open circles indicate the decay kinetics of the 900 nm absorbance in the 0.174 M solution; these are the decay kinetics of the dimer cation. The slow component in the 3.5 and 7.6 mM traces decays in the same way as this 0.174 M trace. In Fig. 30S(b), the rate constant k_1 is for the *fast* components of the biexponential kinetics.

Fig. 31S.

A set of $\Delta\Delta OD_\lambda$ kinetics for neat sc CO_2 (400 to 950 nm) obtained under similar conditions as the three kinetic traces shown in Fig. 10 (E=25 kV/cm). All of these kinetics approach zero after 400 ns. Note that the decay kinetics in the blue are significantly longer than the decay kinetics in the red. For clarity, the $\Delta\Delta OD_\lambda$ kinetics obtained at different wavelengths are stacked on top of each other.

Fig. 32S.

Evolution of the ΔOD_λ *(open circles)* and $\Delta\Delta OD_\lambda$ *(filled cicles)* spectra obtained by time integration of the corresponding kinetics in pulse radiolysis of neat sc CO_2. The time windows are indicated in the plot. The neutral product contributes to the ΔOD_λ spectra but not to $\Delta\Delta OD_\lambda$ spectra. The two prompt spectra (a) obtained in the 11-26 ns window look similar, since the product yield is still small, and both the solvent radical anion and the solvent radical cation exhibit the same field effect on their yield. At later delay times (b,c), the relative contribution from the blue-absorbing solvent radical anion increases (see also Fig. 12(b)) and the product absorbance begins to contribute to the ΔOD_λ spectra. This

© 2002 American Chemical Society, J. Phys. Chem. A, Shkrob jp021494K, Supporting Info Page 29

figure illustrates how the field effect - transient absorbance spectroscopy measurements help to sort out complex optical spectra.

Fig. 33S.

Normalized $\Delta\Delta OD_\lambda$ kinetics in (a) neat sc CO_2 and (b) 0.17 M solution of SF_6 in sc CO_2. The detection wavelengths are given in the plots. Whereas in the SF_6 solution, all kinetics are the same (as only the solvent radical cation contributes to $\Delta\Delta OD$ in this solution), in neat sc CO_2, the kinetics observed at shorter wavelengths are longer than the kinetics observed at λ<850 nm. This due to the composite nature of the absorbance signal: both the solvent radical cation and the solvent radical anion (whose life time is longer) contribute to the observed decay kinetics.

Fig. 34S.

(a) *To the top axis and to the right axis.* Transient absorbance ΔOD_{900} in pulse radiolysis of neat sc CO_2 (cell-1, with beam collimator) as a function of the accumulated dose (see sections 3.3 and 2S.2 for details). The data for pulses with nominal lengths of 4, 10, and 20 ns are plotted together (the time profiles of these pulses are given in Fig. 11(a)). The pulse charge was 30, 67, and 122 nC respectively, and the total dose was 26.3, 59.3, and 106.6 Gy, respectively. The time dependence of the dose accumulation was obtained by integration of the kinetics of Cerenkov emission given in Fig. 11S(a). *To the bottom and to the left axis:* The dependence of the cation yield C(t) (calculated from the ΔOD_{900}) as a function of the total yield of electron-hole pairs, g(t) (calculated from the dose assuming the radiolytic yield of 5 electron-hole pairs per 100 eV of absorbed radiation). The solid line is theoretical dependence given in Fig. 19S (assuming $C_{cr}\approx3.02$ μM); see sections 4.1 and 2S.2 for more detail.

(b) A product $G\varepsilon^+_{750}$ of the radiolytic yield G (in species per 100 eV of absorbed radiation) and the decadic molar extinction coefficient ε^+_{750} of the solvent radical cation in neat sc CO_2 (λ=750 nm is the absorbance maximum of this cation) as a function of the radiation dose. The data obtained using the same three pulse lengths are plotted together. As the dose increases, the apparent yield decreases.

Fig. 35S.

(a) Time evolution of the absorption spectra in pulse radiolysis of neat sc CO_2. On the millisecond time scale, the shoulder at 700 nm steadily increases with the delay time. (b) Effect of addition of carbon monoxide on the λ=550 nm kinetics (0.1-100 ms). The CO concentrations are (i) 0, (ii) 0.1, (iii) 0.23, and (iv) 1.0 M. Analysis of these data indicates that CO scavenges a fraction of the light-absorbing species with rate constant of of ca. 770 $M^{-1}\,s^{-1}$.

Fig. 36S.

Pulse radiolysis of neat sc CO_2. Typical decay kinetics of the 550 nm absorbance on the 100 μs to 2.5 s time scale (for a 67 Gy pulse). (a) Logarithmic time scale. (b) Linear time scale. The bold solid line is the second-order kinetic fit.

© 2002 American Chemical Society, J. Phys. Chem. A, Shkrob jp021494K, Supporting Info Page 30

Fig. 37S.

(a) Transient absorbance kinetics at 550 nm obtained in radiolysis of neat sc CO_2 using a sequence of one, two, and four "10 ns", 67 Gy pulses (30 Hz burst). The absorbance steadily increases after each pulse, and the decay kinetics become faster.

(b) Transient absorbance kinetics at 550 and 900 nm observed on the submillisecond time scale in pulse radiolysis of neat sc CO_2. The delayed formation of the red-absorbing product is clearly observed.

Fig. 38S.

(a) Transient absorbance kinetics at (i) 400, (ii) 500, and (iii) 700 nm observed in neat sc CO_2 during and after a 30 Hz burst of twenty "10 ns", 67 Gy pulses. Traces (iv) and (v) are the signals from the windows (these were subtracted from the kinetic traces (i-iii)), at 400 and 700 nm, respectively. Note the difference between the product accumulation kinetics for traces (i) and (iii). The onset of the exponential growth is λ=600 nm; in the red the growth is linear.

(b) Evolution of the absorption spectra by time integration over pulses number 1-3, 5-6, 10-12, and 14-15 within the same 30 Hz burst of twenty pulses. All these spectra are similar. For comparison, the absorption spectrum of the product obtained by the integration in the 0.5-1 μs window is shown (filled diamonds); this spectrum, appropriately scaled, is also shown by the bold solid line. The comparison suggests that the absorbance in the red is from another species. This conclusion is also supported by the differences in the accumulation dynamics of the absorbances during a pulse burst (see above) and the single-pulse kinetics observed on the submillisecond time scale (Fig. 37S(b)).

Fig. 39S.

Transient absorption spectra obtained in pulse radiolysis of neat sc CO_2 (filled diamonds), and 7.6 mM (filled squares) and 0.175 M (filled circles) solutions of nitrous oxide in sc CO_2. The integration windows are (a) 2-20 ns and (b) 20-45 ns. In plot (b), the open symbols correspond to the spectra obtained by time integration between 0.6 and 1 μs. These spectra are mainly from the stable product. The prompt spectra (a) exhibit the charge resonance band of the $(N_2O)_2^+$ dimer cation that is centered at 650 nm. In the 0.175 M solution, this band is formed instantly. In the 7.6 mM solution, its formation is delayed (compare (a) and (b)). The absorbance at 400-500 nm is from the solvent radical anion. Neither this anion nor its precursor, the quasifree electron, react with N_2O (ref. 4).

Fig. 40S.

Transient absorbance kinetics at (a) 400, (b) 450, and (c) 600 nm obtained in pulse radiolysis of oxygenated solutions of sc CO_2. The oxygen concentrations are 1, 4, 19, and 420 mM (see the color table in the plot). Addition of oxygen results in rapid conversion of the solvent radical cation to CO_4^+ which is a poor light absorber in the visible. Oxygen also react with the solvent anion and its precursor to yield CO_4^- anion whose absorption has an onset at 450 nm. The residual signal at 600 nm (at $[O_2]$=0.42 M) is that of the stable product whose formation kinetics is observed within the first 250 ns. This product does not react with oxygen and its yield does not change upon the addition of oxygen. At 450 nm, both this product and CO_4^- contribute to kinetics (the short-lived "spike" is from the solvent

© 2002 American Chemical Society, J. Phys. Chem. A, Shkrob jp021494K, Supporting Info Page 31

radical cation). At 400 nm, the kinetics do not change with addition of O_2. It is possible that λ=400 nm is a double isosbestic point for the CO_4^- and $(CO_2)_n^-$ anions and the CO_4^+ and $(CO_2)_n^+$ cations.

Fig. 41S.

(a) Full set of transient absorbance kinetics (400 to 700 nm) obtained in pulse radiolysis of 33 mM solution of O_2 in sc CO_2. At this concentration, the solvent radical cation is scavenged within the duration of the electron pulse. For λ<500 nm, the kinetics are dominated by the stable product. (b) Time evolution of the absorbance spectra in the same solution. There are two contributions to these spectra: at short delay time, the absorbance spectrum is mainly from CO_4^-; at later times, the absorption is mainly from the stable product. Even at t<20 ns, some contribution from the product absorption is seen. The absorbance in the 400-450 nm range is probably a red edge of a stronger UV band of the CO_4^- radical.

Fig. 42S.

(a,b) Transient absorption kinetics at 700 nm in pulse radiolysis of neat sc CO_2, 7 mM and 0.21 M solutions of CO in sc CO_2, 0.21 M solution of CO with 7 mM of O_2 added, and 1.7 M solution of H_2 (see the color table in the plot). As the solvent radical cation is scavenged by CO, the residual signal is mainly from the product. This residual kinetics does not change upon the addition of oxygen and is similar to the product accumulation kinetics observed in hydrogenated solutions at the same wavelength.

Fig. 43S.
A family of ΔOD_λ kinetics obtained in the 400 to 650 nm range in pulse radiolysis of of (i) neat sc CO_2, (ii) 7 mM and (iii) 0.24 M solutions of CO in sc CO_2, and (iv) 0.24 M solution of CO with 25 mM of O_2 added (see the color table in the plot for λ=650 nm). In the 550, 600, and 650 nm traces, fast formation of a light-absorbing species is clearly discernible (traces (ii) and (iii)); this formation kinetics is much faster than the formation kinetics of the product (trace (iv) and Fig. 42S). At [CO]=0.24 M, the solvent radical cation is scavenged within the electron pulse and only the formation kinetics of the new light-absorbing species is seen at 550-650 nm. At [CO]=7 mM, these formation kinetics are superimposed on the rapid decay kinetics of the solvent radical anion. Addition of 25 mM O_2 prevents the formation of the 550-650 nm absorbance; only neutral product is seen in the oxygenated solution. Oxygen reacts with both the solvent and the solute radical cations yielding CO_4^+ cation, which is a poor light absorber in the visible. Addition of 1.7 M H_2 has an effect (not shown) similar to addition of O_2 since at this concentration of hydrogen proton transfer reaction (2) occurs nearly as efficiently as the scavenging of the solvent hole by 7 mM CO. We believe that the 550-650 nm absorption results from a charge resonance band in a higher $(CO)_n^+$ multimer cation. This band must be narrow, as rapid formation kinetics are not observed outside the given spectral range (see the 400-500 nm traces in the same plot).

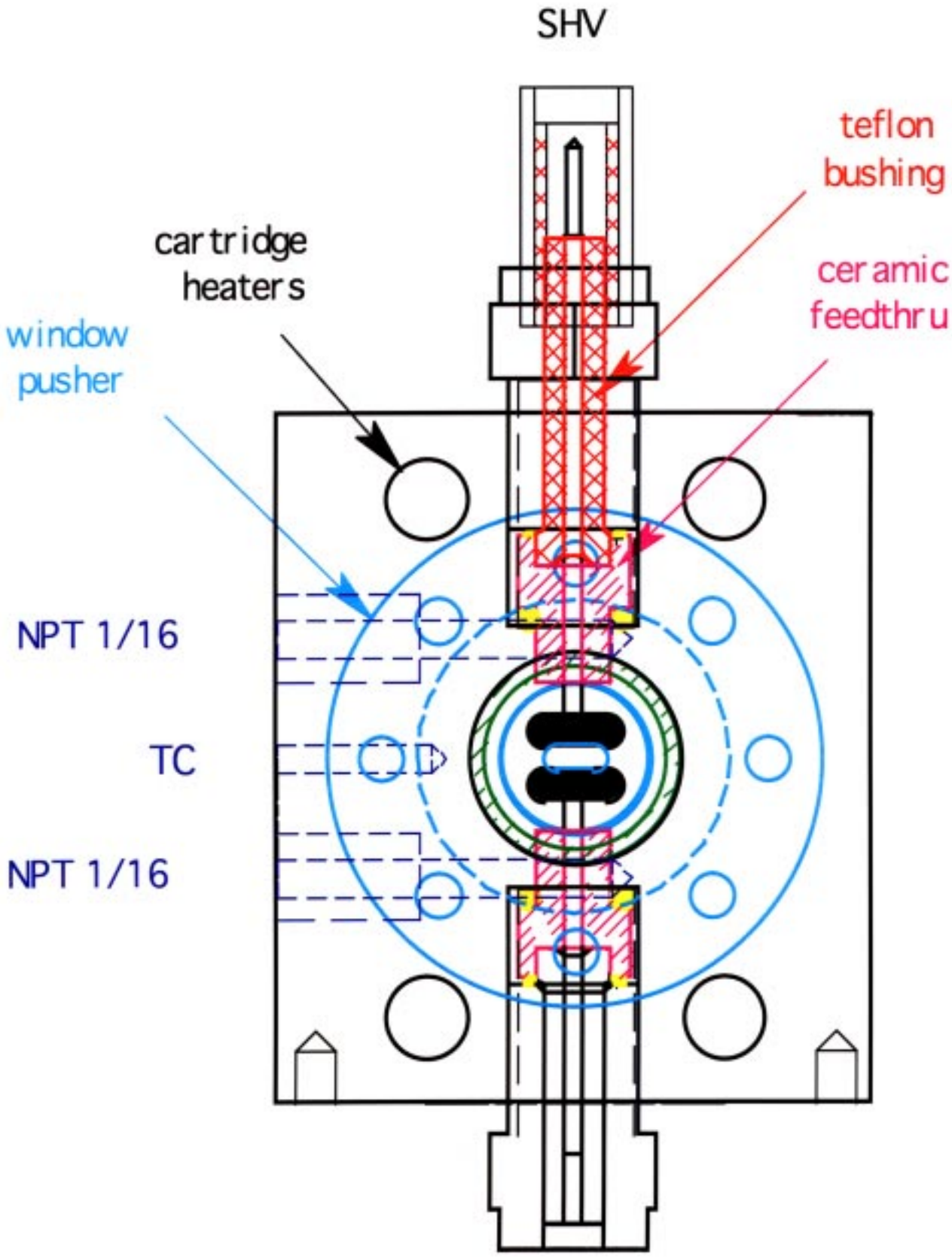

Fig. 1S, Shkrob et al

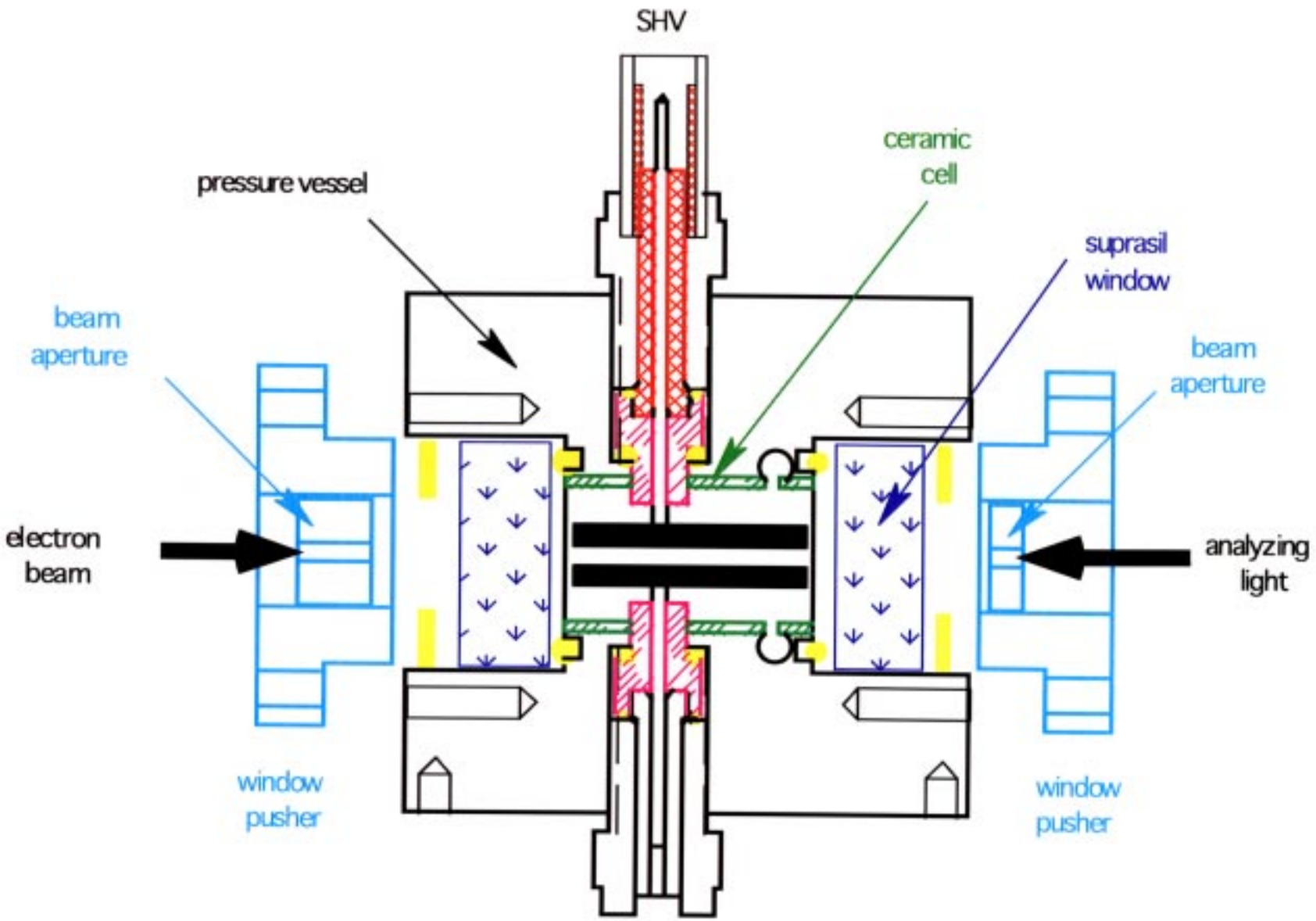

Fig. 2S, Shkrob et al

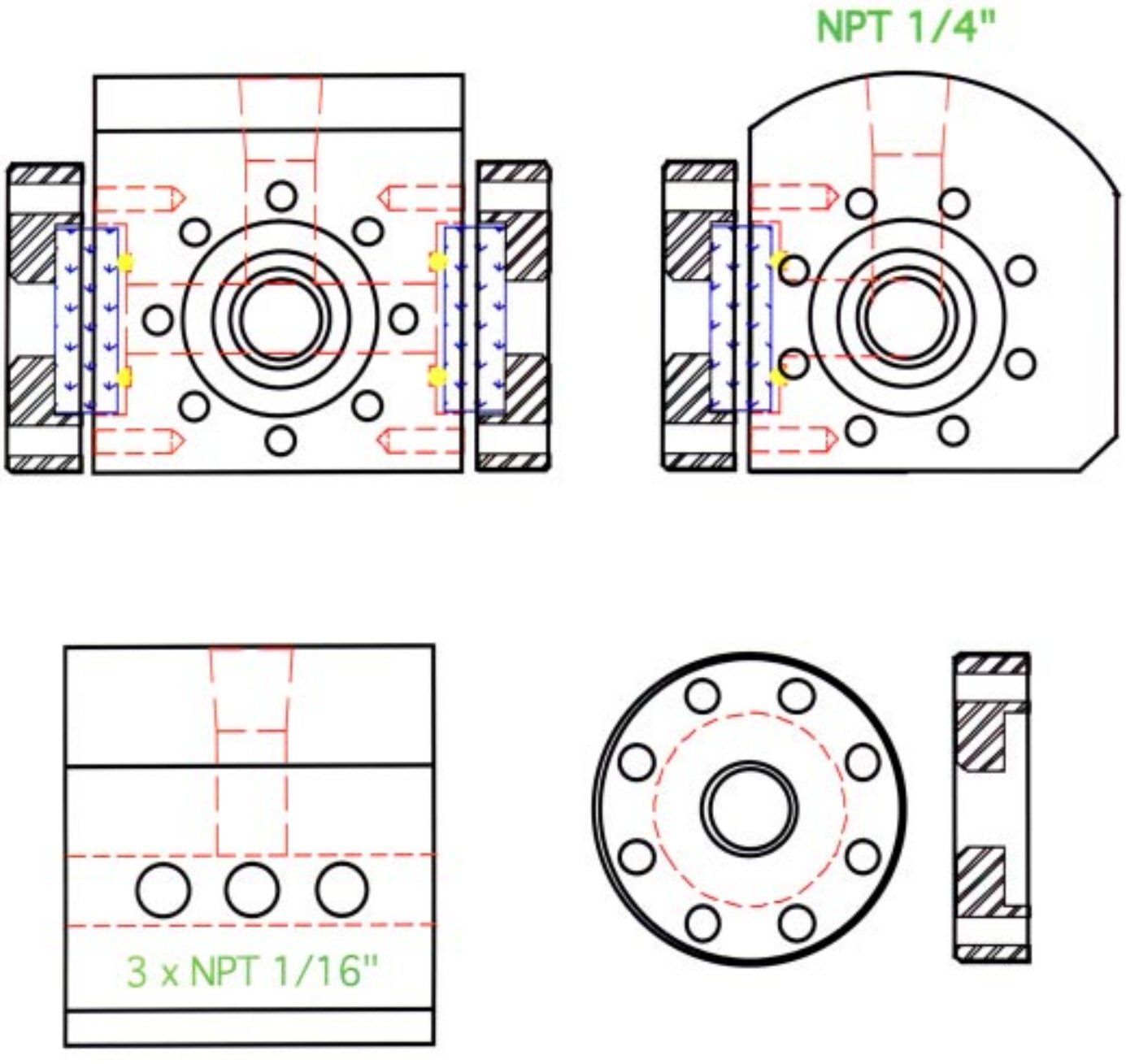

Fig. 3S, Shkrob et al

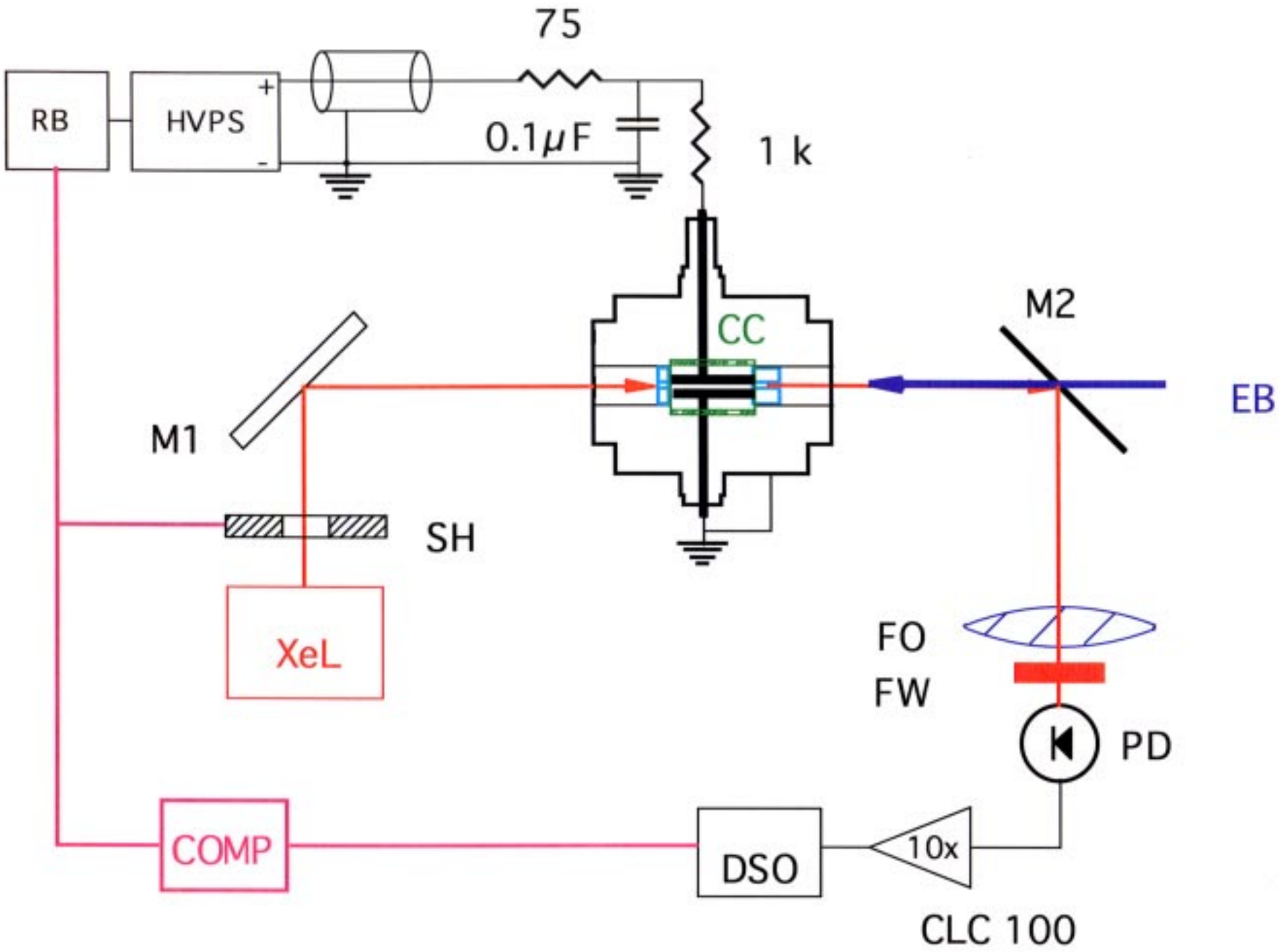

Fig. 4S, Shkrob et al

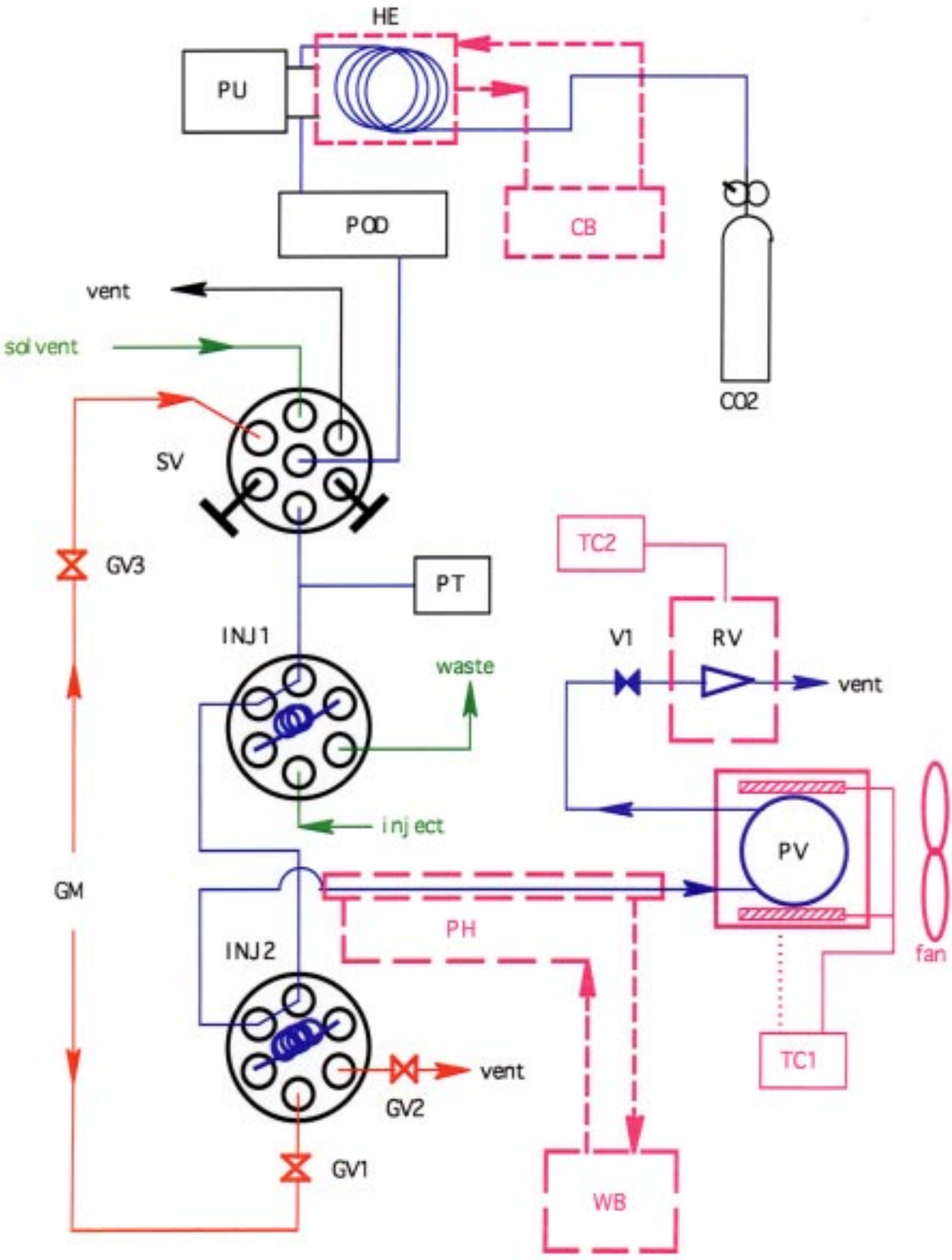

Fig. 5S, Shkrob et al

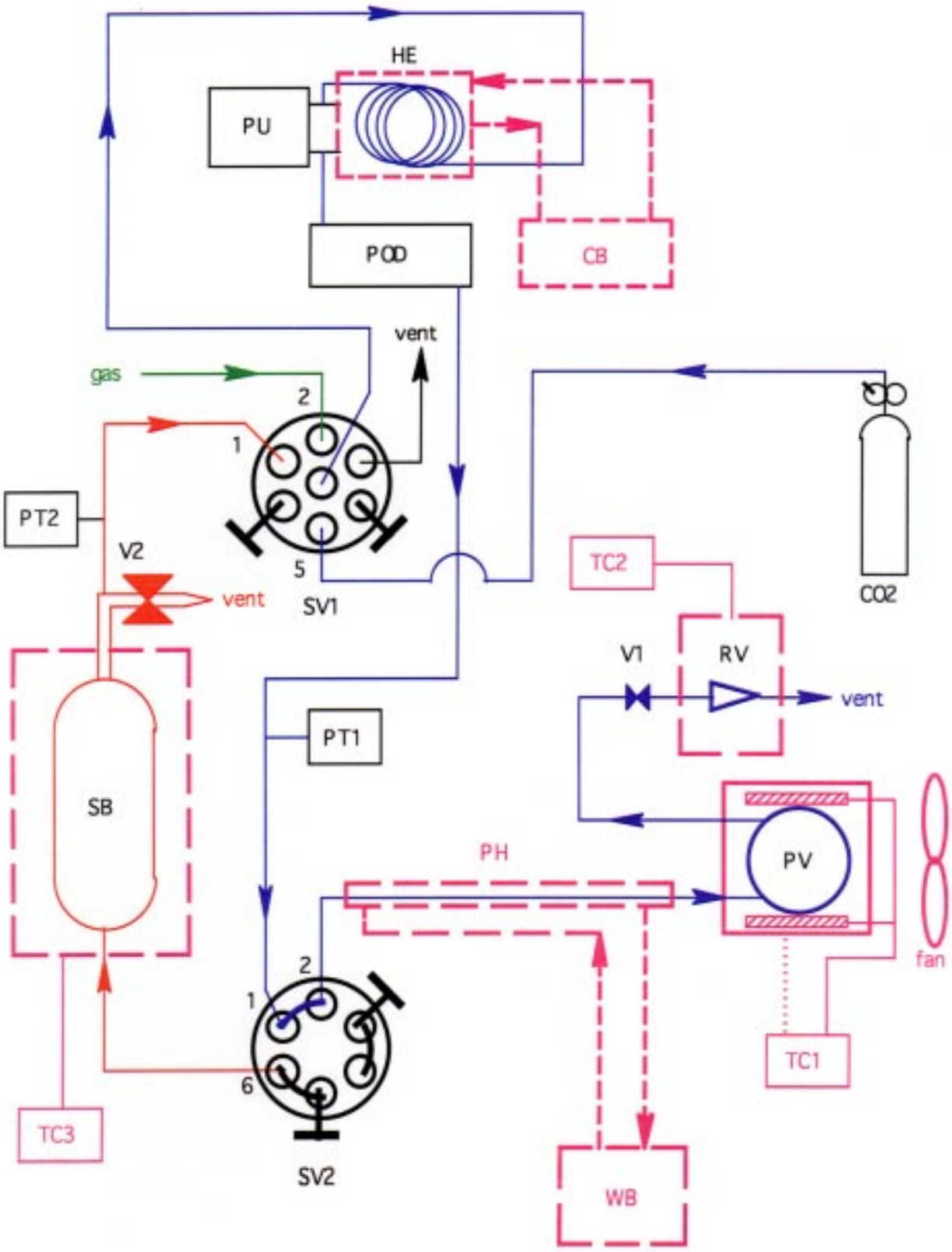

Fig. 6S, Shkrob et al

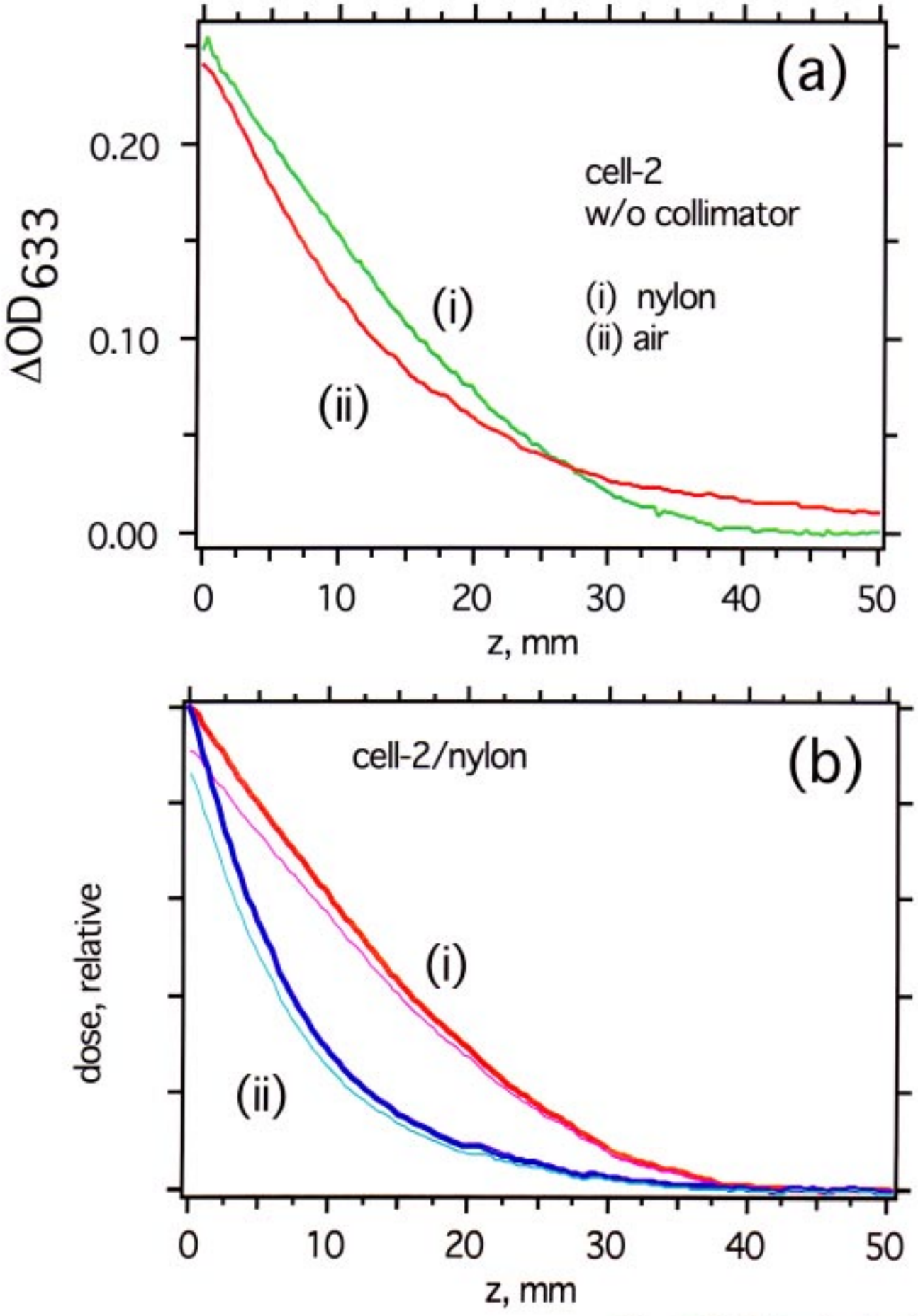

Fig. 7S, Shkrob et al

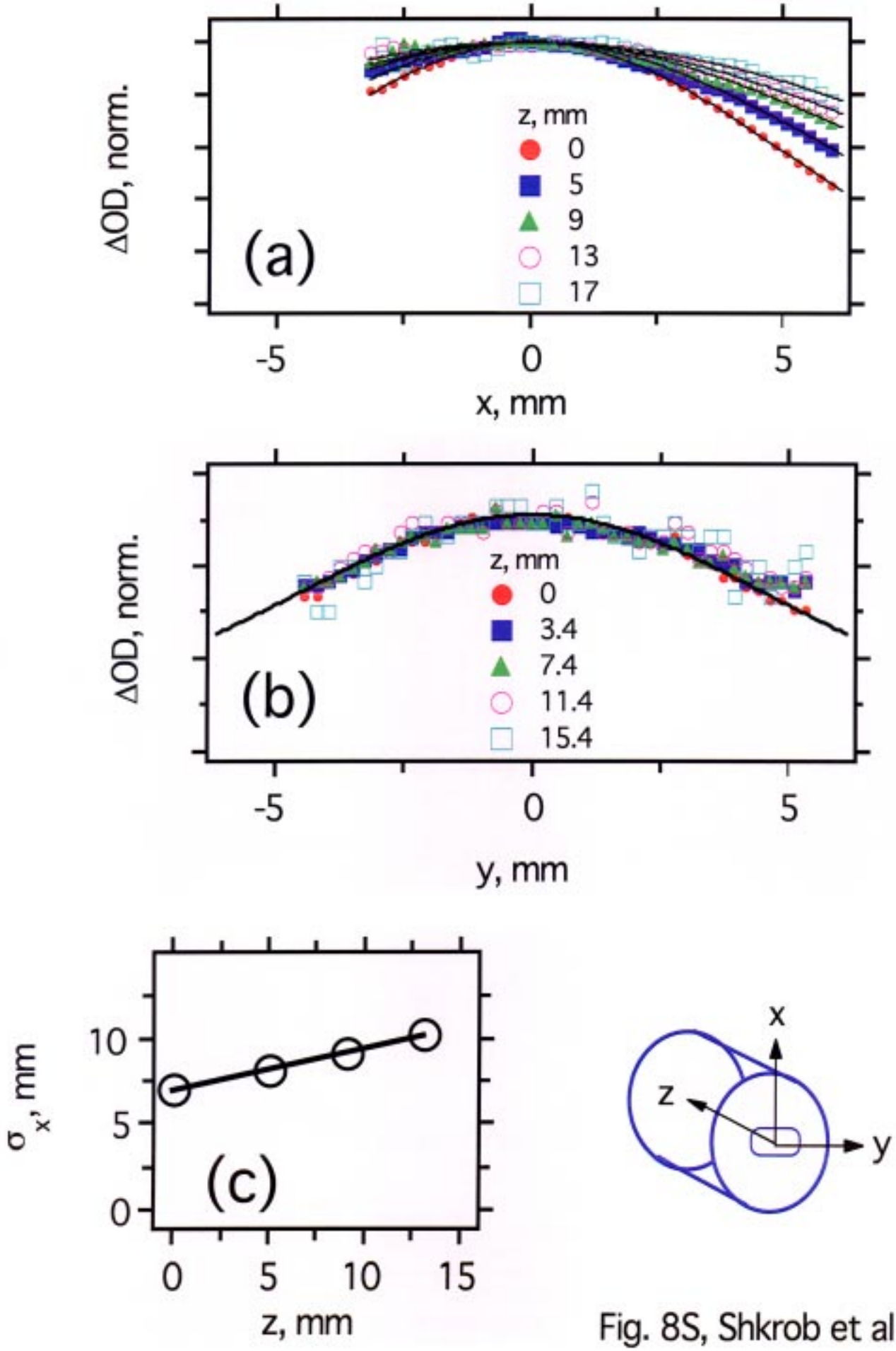

Fig. 8S, Shkrob et al

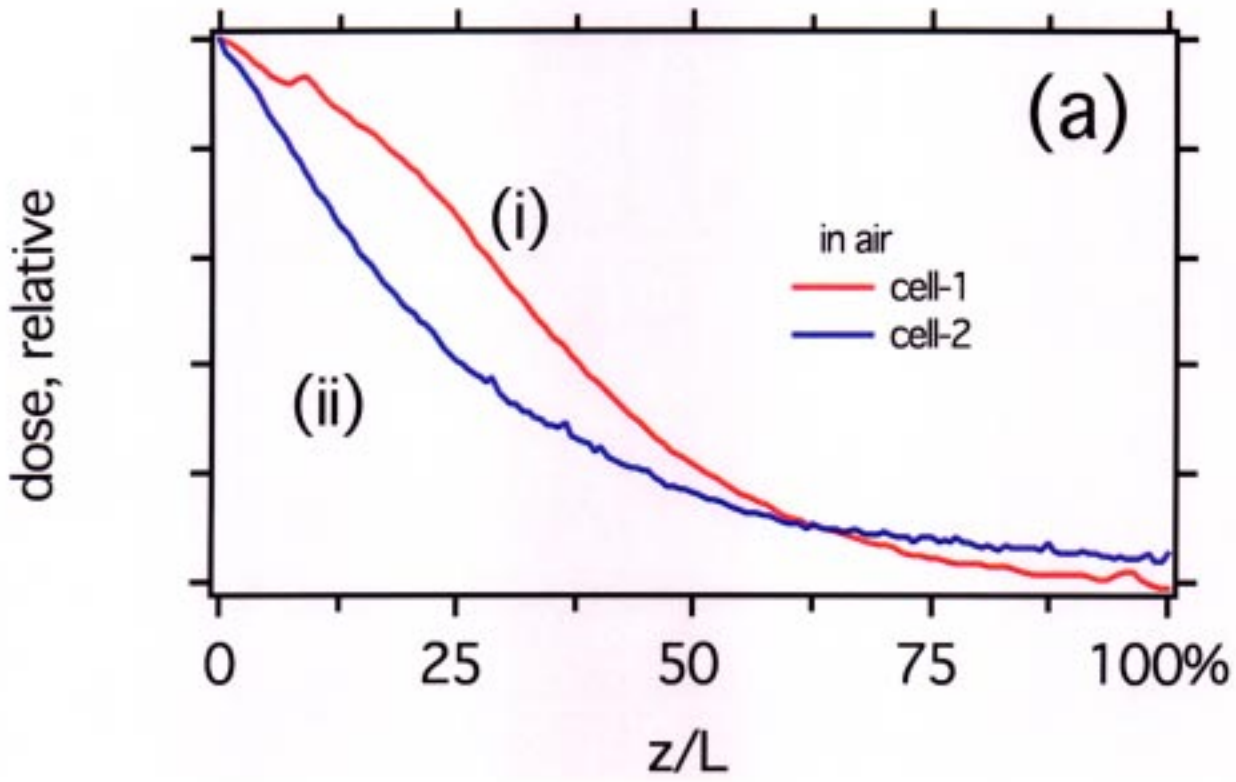

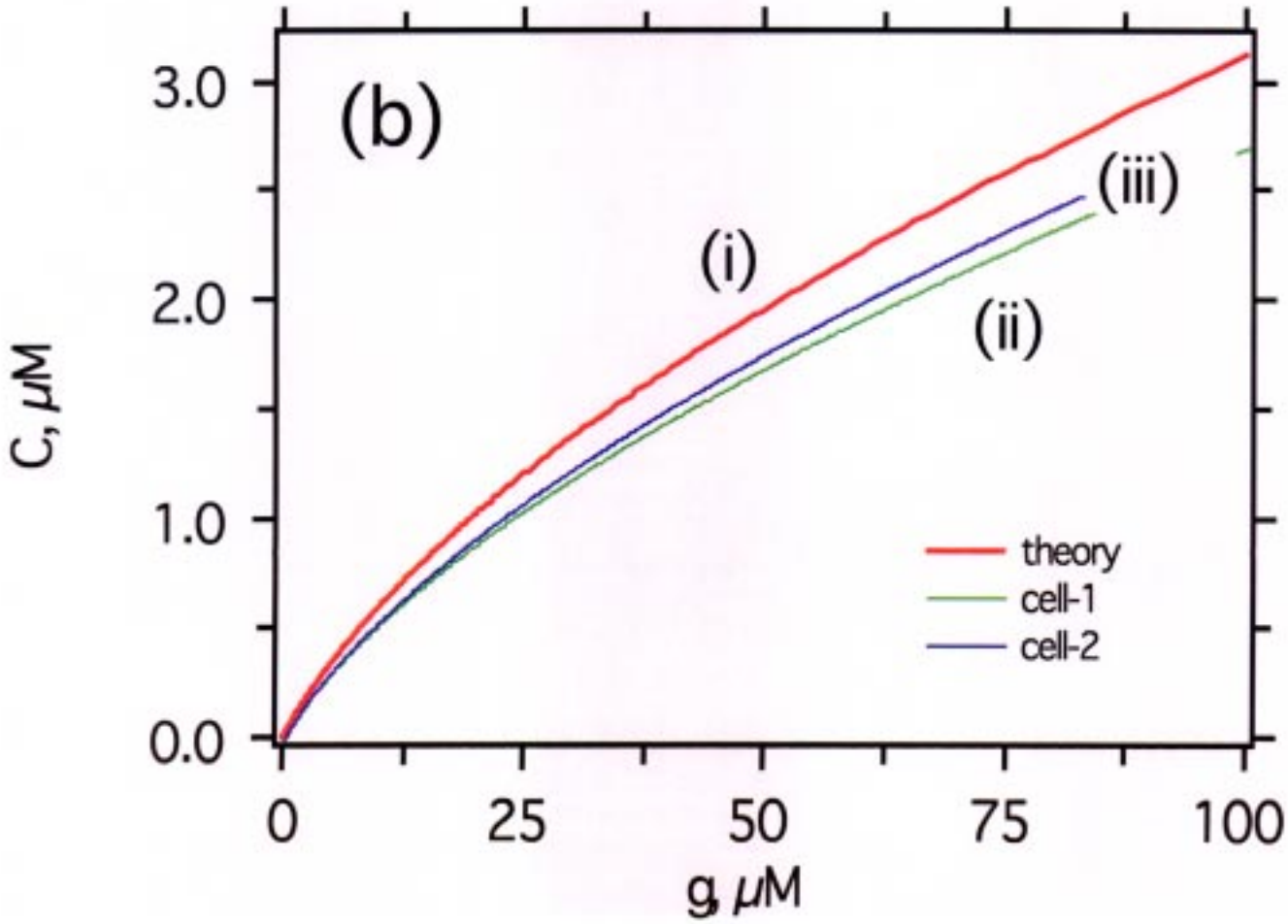

Fig. 9S, Shkrob et al